Spring 4-8-1997

Angle-Resolved Study of Ar $2p_{1/2,3/2}^{-1}$ns,d Resonant Auger Decay

Marc Andrew Humphrey
Western Michigan University, mhumphrey@post.harvard.edu

Angle-Resolved Study of Ar $2p_{1/2,3/2}^{-1}$ns,d Resonant Auger Decay

A thesis submitted to

the Carl and Winifred Lee Honors College,
Western Michigan University

by

Marc Andrew Humphrey

April 8, 1997

Thesis Committee Members:

Dr. Nora Berrah, Chair
Department of Physics, Western Michigan University

Dr. Thomas Gorczyca
Department of Physics, Western Michigan University

Dr. Timothy J. Gay
Department of Physics, University of Nebraska-Lincoln

THE CARL AND WINIFRED LEE HONORS COLLEGE

CERTIFICATE OF ORAL EXAMINATION

Marc Humphrey, having been admitted to the Carl and Winifred Lee Honors College in 1993, successfully presented the Lee Honors College Thesis on April 8, 1997.

The title of the paper is:

"Angle-Resolved Study of Ar $2p_{1/2,3/2}^{-1}$ns,d Resonant Auger Decay"

Dr. Nora Berrah
Physics

Dr. Thomas Gorczyca
Physics

Dr. Timothy J. Gay
Univeristy of Nebraska-Lincoln

Abstract

Angle-resolved measurements of the Ar $2p_{1/2}^{-1}4s,3d,4d$ and $2p_{3/2}^{-1}4s,3d,4d$ resonant Auger transitions have been carried out using photons from an undulator beamline at the Advanced Light Source of Lawrence Berkeley National Laboratory. The intensity distributions and angular distribution anisotropy (β) parameters have been reported for nearly all of the possible $3p^4nl$ final ionic states. These results further verify the predictions of the spectator model for the $2p_{1/2,3/2}^{-1}4s$ resonances and the subsequent breakdown of this model for the $2p_{1/2,3/2}^{-1}3d$ and $2p_{1/2,3/2}^{-1}4d$ relative intensities. This work produced the first report of the resonant Auger β parameters of the $2p_{1/2,3/2}^{-1}3d$ and $2p_{1/2,3/2}^{-1}4d$ resonances and the intensity distribution for the $2p_{1/2}^{-1}4d$ resonance. These results have been compared with previous experimental and theoretical results wherever possible.

Acknowledgments

As I pen the final thoughts to be incorporated into this thesis, and as I draw my undergraduate career to a close, I feel a powerful urge to express my appreciation to a number of people who have helped bring this thesis into existence and to have brought my dreams into reality.

First and foremost I thank Joseph Reish, Dean of the Lee Honors College. Far beyond filling his role as chief organizer at the Honors College, Dr. Reish has been a close friend and inspiration to me. Without much of his help, and all of his caring, many of the modest accomplishments I've reached at Western Michigan University would have never materialized.

Though he appears officially on this document as a Thesis Committee Member, Professor Timothy Gay has become much more to me over the past years. Allowing me a place in his laboratory at the University of Nebraska-Lincoln, Dr. Gay has allowed my education of experimental physics to flourish, and has guided my ambition to reach high, yet achievable, standards.

Also much more deserving than the title Committee Member would boast, Dr. Tom Gorczyca has also aided me far beyond the pages of this text. As a dynamic teacher of a few special classes, Dr. Gorczyca has proven that success can still be reached while maintaining utmost excitement, curiosity, and innocence. From him I have learned the usefulness of always remembering the simplest of physical principles when attempting to solve the most daunting problems.

A similar accolade is expressed to Professor Gerald Hardie. For years Dr. Hardie has taught me that I really can do more, learn more, and above all achieve more than I initially imagined. His excellently prepared lectures and ubiquitous amicability have helped me to develop into a better student.

In many similar ways, a number of other teachers at Western Michigan University have done as much to kindle my imagination as they have to lay my foundation of basic mathematical and physical principles. Professor's Dean Kaul, Paul Pancella, and Clement Burns of the Department of Physics and Professor's Paul Eenigenburg, P. Hsieh, S. F. Kapoor, Arthur White, and Yousef Alavi of the Department of Mathematics have all contributed invaluable components to my educational development.

Three years ago, as an eager, yet unskilled freshman, Dr. Nora Berrah gave me the chance to work in her experimental physics group at Western Michigan University. During the duration of our work together, she has continued to support me, challenge me, and inspire me more and more each year. Above all, I owe her most for all of the many wonderful opportunities I've encountered, and for her endless assistance I am forever endebted. Far from caring solely about my scientific development, Dr. Berrah has taught me how to become a better human being, and I only hope one day I will make her as proud of me as I am of her.

Several members of the team which contributed significantly to this work must also be acknowledged. Ahmad Farhat provided many hours of labor and discussion and greatly helped to make this work more complete.

Similarly, Ant Wills was always available whenever I needed assistance. Finally, without the brilliance and hard work of Burkhard Langer or John Bozek this work would have never even begun, let alone reached completion.

I wish to thank Russell and Eloise Seibert for the many priceless gifts they have offered me while at WMU. Far beyond their generous donation of my Medallion Scholarship, they have invested an interest in my personal life and my educational progress that is much more valuable. I could never truly express my appreciation to them.

Above all, I wish to acknowledge the endless support I have received from my parents Steve and Ruthann, and my elder brother Craig. When times were hard, they helped me to stand; and when times were at their best, they were always the most excited to hear. Their influence on me as a human being, and their constant interest in my educational progress have often been the only thing to help me move on. I wish to thank my loving family for making my life a dream, and my dreams a reality.

Table of contents

Abstract....ii
Acknowledgments....iii
Table of contents....v
I. Introduction....1
1. Atomic physics....1
2. Determination of atomic structure and dynamics....2
3. Photoelectron spectroscopy using synchrotron radiation....2
II. Theoretical background....4
1. Resonant Auger processes....4
2. Angular distribution....5
3. Previous studies of Auger decay in noble gases....7
4. This work....8
III. Experimental apparatus....9
1. Synchrotron radiation....9
2. Time-of-flight spectroscopy....11
3. Experimental setup....12
4. Data collection and analysis....14
IV. Results and discussion....17
1. The $2p^{-1}4s$ resonant spectra....17
2. The $2p^{-1}3d$ resonant spectra....23
3. The $2p^{-1}4d$ resonant spectra....27
V. Conclusions....31
VI. References....32

I. Introduction

1. Atomic physics

From the simplest actions like lighting a lamp, to procedures as complex as performing laser surgery, the properties and effects of atoms are a ubiquitous component to our daily lives. The existence of atoms has been speculated on for over two millennia. The first recorded reflection on the particle nature of matter was made by the Greek scholar Democritus, who believed there was a level of matter indivisible even with an infinitely sharp knife. This fundamental unit he termed "atomos," literally Greek for "indivisible." [1]

Democritus' vision laid dormant for centuries until a set of postulates was developed by the British chemist John Dalton (1766-1844) who also proposed that all matter is composed of indivisible atoms. Physical evidence, in the form of conservation of mass and the law of multiple proportions, supported these claims [2]. Once reasonable evidence was established regarding the existence of atoms, many studies followed to try and understand their structure and many atomic models were subsequently developed. Hypotheses such as Thomson's plum pudding model (1898), Rutherford's nuclear model (1910), and Bohr's theory (1913) have lead to an understanding of the chemical elements incorporated in the Periodic Table as well as the realization that atoms, initially thought to be indivisible, were in reality composed of the more fundamental subatomic particles: protons, neutrons, and electrons [3].

The study of atoms is one of the main branches of physics, and the field itself is very broad. Discerning atomic structure and dynamics is the primary focus of such fields as electron and ion scattering, laser spectroscopy, or synchrotron radiation spectroscopy (the subject of this work). Other studies use atoms as tools to make precision measurements of fundamental constants, for example, through the use of a laser technique known as optical pumping, where certain energy states of atoms are isolated and probed by laser radiation. A more recent development in atomic physics, namely laser cooling and trapping, utilizes lasers and magnetic fields to localize atoms in space and reduce their temperatures to record lows. This area of research gives physicists a new way to look at old problems (i.e. with colder atoms) and also allows a new state of matter, a Bose-Einstein condensate, to be produced and studied. In addition to these areas of fundamental research, the study of atoms has also been used in many practical applications. Two of the many relevant examples are the development of lasers for surgery and communication, and novel biomedical imaging techniques (namely MRI) using spin polarized atomic vapors. As has been evidenced by numerous advances in communications, medicine, and scientific instrumentation, an understanding of atoms is clearly of fundamental importance.

2. Determination of atomic structure and dynamics

It was once said that the best way to learn how a clock works is to throw it against a wall and observe what comes out and how. This description, though very crude, is surprisingly accurate in describing the large branch of collisional atomic physics. In this area, physicists bombard atomic targets with ions, electrons, or other atoms. A very elegant approach has also emerged using instead a beam of electromagnetic radiation to disrupt an atom to observe the resulting dynamics. Since the forces that bind the electrons to its nuclear core are electromagnetic in nature, the introduction of an external electromagnetic field causes an atom to change structure under the introduced perturbation. By observing the rate and mode of change, insight can be extracted into atomic structure, and empirical models can be developed to try and explain such observed phenomena as photoabsorption, photoemission, and ionization.

One type of probe that has become extremely important to the study of atoms is synchrotron radiation. A more detailed description of synchrotron radiation sources is given in Chapter III. In the past decade, synchrotron sources have blossomed as useful tools used by researchers in many different fields. For example, chemists use these sources to study the time evolution of chemical reactions. Biologists use them to map out structure at levels ranging form macromolecules to cells to microscopic organisms, such as the malaria parasite. Materials scientists also use synchrotron radiation to develop more efficient semiconductors or integrated circuits. In addition to these studies, a new program of experiments investigating atomic and molecular structure and transition processes has become possible. Researchers have studied the effects of photon bombardment of atoms during and after the interaction; a new understanding of the complex structure and dynamics of multielectron atoms is thus being gained [4].

3. Photoelectron spectroscopy using synchrotron radiation

When a low energy photon ($h\nu < 0.5$ MeV) from a synchrotron source impinges on an atom, a process known as the photoelectric effect is very likely to occur. In this process, the incident photon transfers all of its energy to an atomic electron, thereby causing a photoexcitation or photoionization event [5]. By measuring the kinetic energy E_K of an electron ejected by a photon of well defined energy, the state of the ion left behind, characterized by a unique binding energy E_B, can be determined through the relation

$$h\nu = E_K + E_B, \tag{1}$$

which is simply an expression of the conservation of energy [6]. A schematic showing two representations of this process is given in Figure 1 [7]. The method of measuring the number of electrons ejected at different discrete energies is known as photoelectron spectroscopy. This method yields an abundance of information about the

likelihood of different transitions in atoms, and allows researchers to learn more about atomic structure and transition processes.

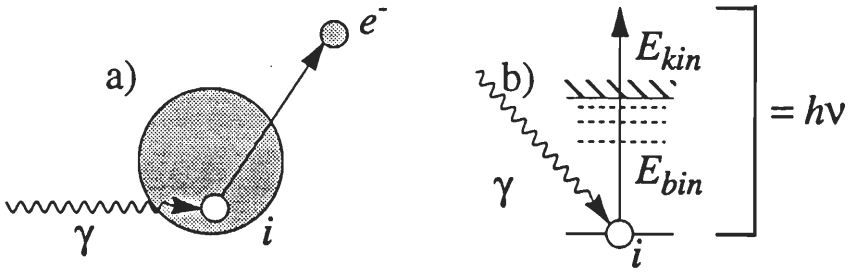

Figure 1. Schematic depicting the process of photoionization. An incident photon of energy $h\nu$ impinges on an atom in state *i*. The result depicted here is the ejection of a photoelectron with kinetic energy E_K. As described by equation (1), the binding energy of the electron is then given as $E_B = h\nu - E_K$. Figure (a) shows a spatial representation of this process while (b) shows the process on an energy level diagram. This figure is reproduced from reference [7].

An experimental approach, such as photoelectron spectroscopy, is necessary in order to learn more about most atoms for the following reasons. The simplest stable atom is hydrogen, consisting of a single electron and a proton. Using the mathematical formalism of quantum mechanics, the behavior of this atom can be modeled to high accuracy. The next simplest atom is helium. A He atom consists of a nucleus (two protons and two neutrons) surrounded by two electrons. If the nucleus is considered to be a single compound body, this system can be treated as a nucleus of charge +2e orbited by two electrons each of charge -1e. Within this representation, however, the atom now consists of a three particle system, and the addition of the third body makes an exact mathematical description unobtainable. As a result, approximations must be made to find a mathematical model. This effort is further complicated by various effects, such as the coupling of orbital angular momentum and spin, which must be considered for multielectron atoms. The end result is an inability to model the atom analytically. Clearly, this same difficulty is present in other multielectron atoms, consisting of an increasing number of electrons, protons and neutrons. In order to understand the processes present in these more complex atoms, an atomic physicist's approach must consist of a coupled progression of theory and experiment. Although the experimental and theoretical tools used are constantly improving, there are many fundamental ideas still not understood. This work is an experimental effort to understand the role of electron-electron correlation in multielectron atoms. The structure and dynamics of the argon atom, observed by exciting an inner shell electron and witnessing the subsequent decay, is studied, and a comparison is made to some of the current theoretical predictions.

II. Theoretical background

1. Resonant Auger processes

When an incident photon excites an inner shell electron to a higher orbital, the excited atom may nonradiatively decay by the ejection of an electron. The ejected electron is called a resonant Auger electron, and this process is termed resonant Auger decay [7]. An alternative process, called normal Auger decay, involves the ejection of an inner-shell electron into the continuum followed by the decay of another electron to the inner shell vacancy and the simultaneous ejection of a second electron, leaving a doubly ionized ion core [8].

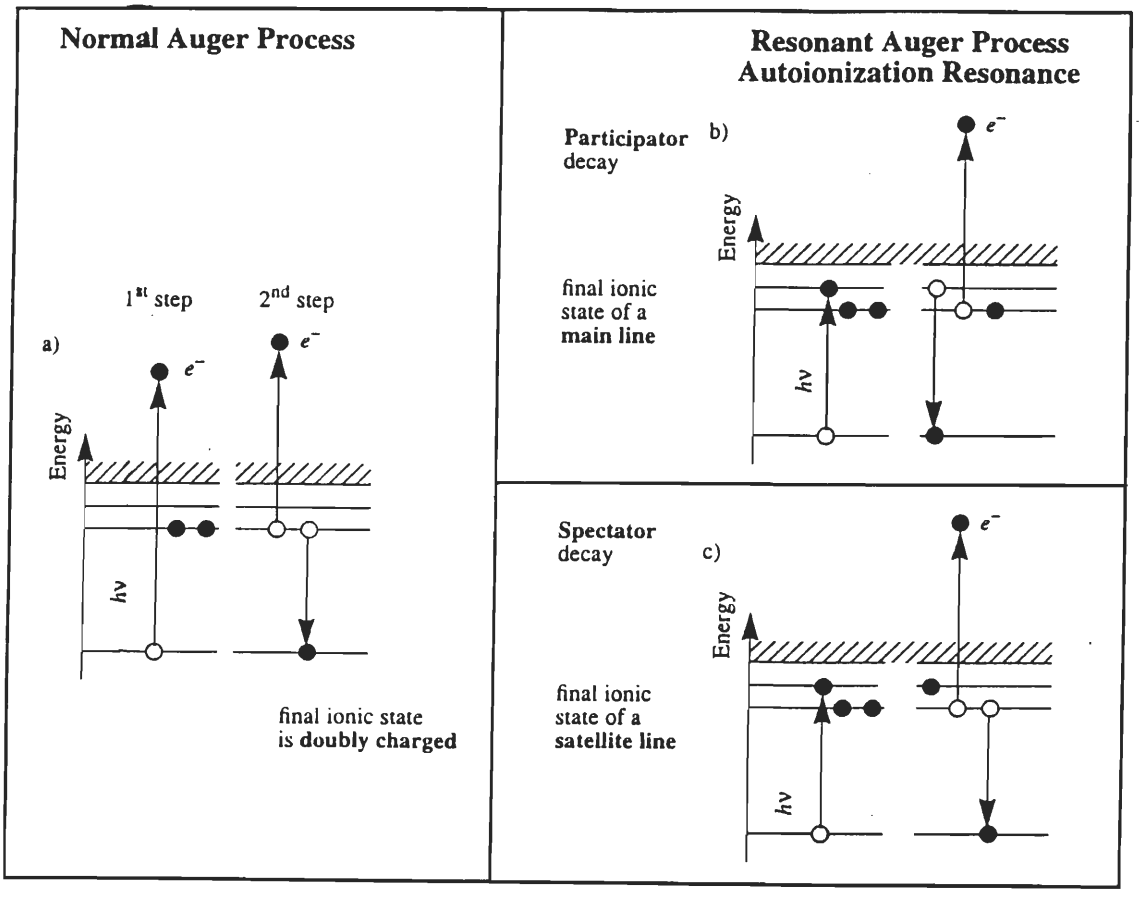

Figure 2. Schematic contrasting Auger processes. The left half of the diagram (a) shows a normal Auger process in which a photon ejects an inner shell electron. A higher orbital electron then fills the vacancy and in doing so ejects a second electron. The right half of the diagram (b,c) shows a resonant Auger decay. In this case, the original electron is not ejected but excited to an outer orbital. The decay is then much like the normal Auger decay, resulting in the ejection of an electron. If the originally excited electron drops down to fill the vacancy this process is termed "participator decay." If, however, the originally excited electron remains in its excited orbital and "observes" the decay of another electron, the process is termed "spectator decay." This figure is adapted from reference [7].

Resonant Auger decay is classified into the following two types. If the originally excited electron decays back to the inner shell hole, the decay is known as participator Auger decay. On the other hand, if the excited electron remains in its original orbital while one of the lower-lying electrons fills the inner-shell hole and another escapes, the process is termed spectator Auger decay [7]. These three processes are summarized in Figure 2 [7]. The electronic configuration for a ground state Ar atom is $1s^2 2s^2 2p^6 3s^2 3p^6$, which can be abbreviated by $2p^6 3l^8$. A common notation to depict the absence of, for example, a 2p electron is $2p^5$nl or $2p^{-1}$nl, where n and l refer to the principle and orbital angular momentum quantum numbers of the excited electron's orbital. Adopting this notation, the resonant Auger processes are further classified here for the Ar $2p^{-1}4s$ resonance:

Spectator Auger decay: $$2p^{-1}4s \rightarrow 2p^6 3l^6 4s + e^- \quad (2)$$

Participator Auger decay: $$2p^{-1}4s \rightarrow 2p^6 3l^7 + e^- \quad (3)$$

Participator Auger decay-shake up: $$2p^{-1}4s \rightarrow 2p^6 3l^6 4p + e^- \quad (4)$$

Participator Auger decay-shake off: $$2p^{-1}4s \rightarrow 2p^6 3l^6 + 2e^- \quad (5)$$

There have been several attempts to theoretically describe these transitions. Some models have treated the Auger decay as a single step [9], while others consider it a sequence of two steps [10-12]. The most prominent to this thesis is the spectator model [10] which assumes the dominant type of decay would be spectator decay. Once the original electron is resonantly excited, this model treats the subsequent decay as a normal Auger decay with the exception of a single electron in a higher orbital. The effect of this electron is to simply reduce the effective potential felt by the ejected electron. No further interaction between the higher lying electron with the ion core or the ejected electron is considered. Using this interpretation, a resonant Auger decay spectra would resemble a normal Auger decay spectra with the only exception of a constant energy shift due to the reduced potential.

2. Angular distribution

When conducting photoelectron spectroscopic studies, various types of information can be determined. The most direct is the number and kinetic energy of the ejected electrons for a particular angle. This type of information yields a quantitative measure of the relative likelihood of different decay modes since, for a well defined photon energy, the kinetic energy of an ejected electron is unique to the final ionic state. Another source of information is the angular distribution of these ejected electrons. This type of study, with its added degree of complexity, requires measurements at more than one angle. To enable this, the measurements described in this thesis were made using two spectrometers mounted on a cylindrical, rotatable vacuum chamber.

In a photoionization process (using the dipole approximation), the differential cross section for the electrons, emitted at an angle θ with respect to the electric field vector in a plane perpendicular to the incident radiation, is given by

$$\frac{d\sigma_{if}(h\nu)}{d\Omega}(\theta) = \frac{\sigma_{if}(h\nu)}{4\pi}\left\{1 + \frac{\beta_{if}(h\nu)}{4}[1 + 3P_1\cos(2(\theta - \lambda))]\right\}, \quad (6)$$

where σ_{if} is the partial cross section, β is the angular distribution anisotropy parameter, P_1 is the degree of linear polarization of the monochromatic light (0.99 in this case), and λ is the tilt angle between the synchrotron plane and the electric field (0 degrees in this case) [14]. This relation shows that the differential cross section exhibits an angular dependence around a plane perpendicular to the incident radiation. Furthermore, it can be seen that the degree of angular dependence is dictated by a parameter β known as the angular distribution anisotropy parameter. Special note should be taken of the angle $\theta_m = 54.7^\circ$ (the magic angle). When this value is substituted into the above equation the angular dependence drops out completely (for P_1 = 1.00, $\lambda = 0^\circ$); in other words, the differential cross section is independent of β at this angle. By making measurements at two different angles, the β parameter can be determined. In particular, if measurements are made simultaneously at the magic angle and 0 degrees, the experimental values can be combined with equation (6) to yield the explicit result for β:

$$\beta(h\nu) = \frac{1}{Eff(h\nu - E_B)}\left(\frac{Cts_0(h\nu)}{Cts_{54.7}(h\nu)}\right) - 1, \quad (7)$$

where Eff represents the relative efficiency (spectrometer transmission as a function of kinetic energy) of the detectors, Cts_0 is the area of the Gaussian curve fitted to the peak measured at zero degree, $Cts_{54.7}$ is the analogous area at the magic angle and E_B is the binding energy for the final ionic state under study. (This equation assumes 100% linear polarization and a tilt angle of 0 degrees). In this study, the efficiency was calculated by making a measurement of the 2s and 2p states of neon and using their known β parameters. With this relationship, one can extract the β parameter for an ejected electron that left the atom in a unique final ionic state. It can be seen from equation 6 that in order for the differential cross section to remain positive, β must range between -1 and 2, signifying the enhancement or reduction of the differential cross section as a function of θ. Figure 3 displays a polar plot of the differential cross section for several different β parameters, assuming 100% linear polarization and a tilt angle of 0 degrees [15]. This figure is cylindrically symmetric about the electric field vector. Here, the independence of the cross section on the β parameter, at the magic angle, becomes apparent as all curves intersect at a single point. The physical significance of β can also be seen by this figure. With β=2, most electron emission is in the direction of the electric field vector, β=0 implies isotropic emission, and β=-1 implies emission perpendicular to the electric field vector.

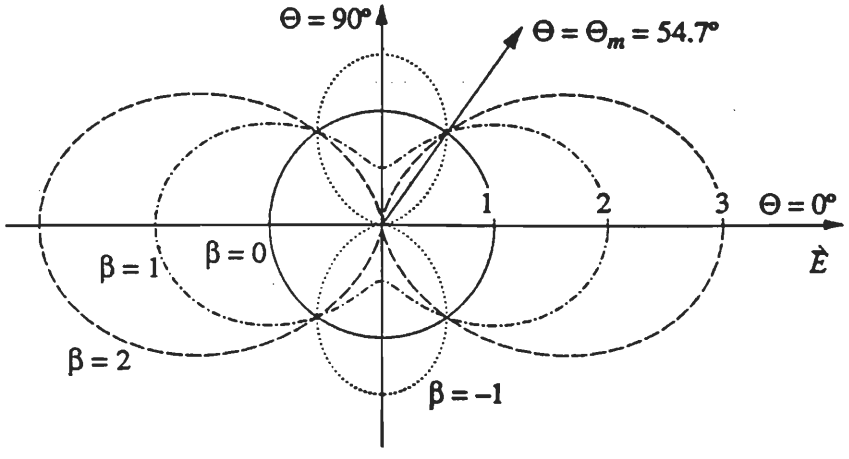

Figure 3. Polar plot of differential cross section for several values of β. In three dimensions, this plot is cylindrically symmetric about the electric field vector shown along $\theta = 0°$. It can be seen that for positive values of β, the preferred direction of electron emission is along the electric field vector, while for negative values of β, the preferred direction is perpendicular to the electric field vector. Isotropic emission can be seen for $\beta=0$. Note that ejection at the magic angle is independent of the β parameter. This figure was taken from reference [15].

3. Previous studies of Auger decay in noble gases

The Auger decay of core excited states in rare gases has been subject to rather intense investigation over a number of years. To briefly summarize some of this work, the $4d^{-1}np$ resonances in Xe have been studied [16-20] with particular attention focused on the role of shake up and shake off processes [16]. Similar work has been performed on the Ar $2p^{-1}nl$ transitions [13,19,21-28] (described in more detail below). Angular distributions have been measured for the Xe $4d^{-1}6p$ and $4d^{-1}7p$ resonances [20,22,29-31] and low resolution angle-resolved measurements of Ar, Kr, and Xe were reported by Carlson et. al. [22]. Theoretical studies have also been made on Ar [9,10,12,13,25], Kr [10-12] and Xe [10-12].

In previous non-angle-resolved studies of the intensity distributions, it has been reported that the decay of the Ar $2p^{-1}4s$ states can be adequately described by the spectator model, while the decays of the Ar $2p^{-1}3d$ and $2p^{-1}4d$ states are dominated by shake up (participator) processes [13,19,21,23-25,27]. Previous angle-resolved measurements of Auger decay, observed at the $2p^{-1}4s$ resonance, suffered from poor resolution in the photoelectron spectra [22]; and angle-resolved measurements of the $2p^{-1}3d$ and $2p^{-1}4d$ resonances have been unobtainable due to insufficient photon resolution.

The Auger decay of the Ar $2p^{-1}4s$ resonances were first described theoretically by Cooper [9], who applied angular momentum transfer theory and treated the resonant decay as a single-step process. Hergenhahn et. al. [10], using the spectator model, treated the resonant Auger decay as a two step process involving excitation and subsequent Auger decay. Chen [11] has shown the importance of including the effect of intermediate coupling in

the calculation of angular distributions of the $2p^{-1}$ hole of normal Auger decay. Later, using the multiconfiguration Dirac-Fock (MCDF) method, in a two step model, Chen [12] reported calculations of the angular anisotropy of the $2p^{-1}4s$ resonant Auger decays.

4. This work

In this thesis, measurements of the intensity distributions and angular distributions for the Auger decay spectra following the $2p^{-1}4s$, 3d, and 4d resonant excitations in argon are reported. These were made in September of 1995 using the high flux and high photon resolution provided by the Advanced Light Source (ALS) along with two time-of-flight (TOF) spectrometers. This work focuses on an analysis of the decay of the $2p_{1/2,3/2}^{-1}4s$, 3d, and 4d states and reports on the relative intensities and angular distribution anisotropy parameters (β parameters) of nearly all possible $3p^4nl$ final ionic states. In the case of the $2p^{-1}3d$, and $2p^{-1}4d$ resonances, the angular resolved measurements were first reported with this effort [32], as was the intensity distribution for the $2p_{1/2}^{-1}4d$ resonance. These results, when compared with theoretical work, demonstrate best agreement with the two-step process calculations, thus pointing out that the separate treatment of excitation and decay mechanisms is justified.

III. Experimental apparatus

1. Synchrotron radiation

The data for this experiment were collected using photoelectron spectroscopy with synchrotron radiation. When a charged particle is accelerated it emits electromagnetic radiation. This process is employed at synchrotron sources, where a beam of high energy electrons is passed through a number of accelerating devices, subsequently releasing a beam of photons [33]. Properties of synchrotron radiation sources which make them ideal for atomic and molecular physics are the high degree of linear polarization of the radiation, the high intensity of photons, and the wide tunability of the photon energy [34].

The history of synchrotron sources is an interesting evolution of efforts attempting to extract the highest quality photon beam from a beam of charged particles. This history is broken down into a number of generations. The first extraction of synchrotron radiation from a synchrotron source was made in 1963. These first efforts were performed using synchrotrons designed for electron or positron scattering experiments. Since the extraction of radiation from such a beam relied on sources already being used for high energy physics, it was termed "parasitic" use. These earliest beams had typical photon fluxes of 10^6 to 10^8 photons per second which were mainly used for photoabsorption measurements. Over the next decade, further development occurred and improvements were witnessed in part through the use of new, ultra-high vacuum capabilities. Subsequently, photon fluxes of 10^{10} to 10^{11} became available and the bandwidths were improved to approximately 1%. (Bandwidth, or photon resolution, refers to the energy spread, or uncertainty, in the photon energy; a higher resolution/narrower bandwidth corresponds to a more well-defined photon energy). With these new sources, a phase of exploratory experiments emerged where the abilities and limitations of synchrotron radiation sources were investigated [35].

In the 1980's, the second generation of synchrotron radiation sources appeared. These new machines were the first built exclusively for the production of synchrotron radiation, a mode referred to as "dedicated" use. These new storage rings produced radiation by passing an electron or positron beam through "bending magnets." The sudden change in direction caused by the bending magnet produced a photon beam with resolution sufficient to study more complex features such as two-electron processes in atoms, autoionization resonances, and photoexcited Auger effects. Another emergent feature of this period was the exploration of insertion devices, placed into straight sections of the storage ring, which were capable of producing much higher resolution photons [35].

These new insertion devices, namely "wigglers" and "undulators," are what characterize the current (third) generation synchrotron radiation sources [35]. In general, these insertion devices are a linear array of magnetic dipoles with alternating polarities, producing magnetic fields perpendicular to the beam propagation direction, and thereby causing a back and forth motion perpendicular to the propagation. The electron motion in an insertion device is characterized by a K parameter which measures the maximum angular deflection of the electron path as a result of magnetic field strength and the spacing between dipoles. In a "wiggler," with $K > 1$,

the radiation will add incoherently creating a wide bandwidth similar to that produced by a bending magnet. The brightness of the beam in this case increases with the number of poles, and a coarse determination of the photon energy region is tuned with magnetic field strength [34]. In an "undulator," with $K \leq 1$, the radiation interferes coherently, producing sharp peaks with narrow bandwidths. In this case, the coarse adjustment of the photon energy window available is determined by varying the physical gap between the poles [34]. An undulator schematic is shown in Figure 4 [33].

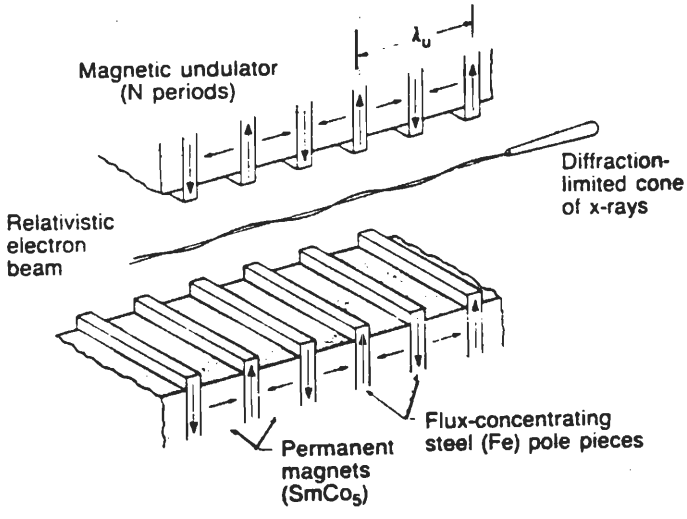

Figure 4. Schematic rendition of an "undulator." The alternating pairs of north/south magnets causes the electron beam to rapidly accelerate back and forth in a plane perpendicular to the magnetic poles. The acceleration leads to the emission of coherent photons with narrow bandwidths. This figure is reproduced from reference [33].

A comparison of photon energy spectra for a bending magnet, wiggler, and undulator is shown in Figure 5 [33]. This latest generation of synchrotron sources typically delivers photon fluxes of 10^{13} photons per second with a bandwidth less than 300 meV (less than 0.1 %). Studies of processes such as low cross section processes, multiple photoionization of atoms, photoionization of singly and multiply charged ions, and photoexcitation studies of inner shell electrons are now possible [35].

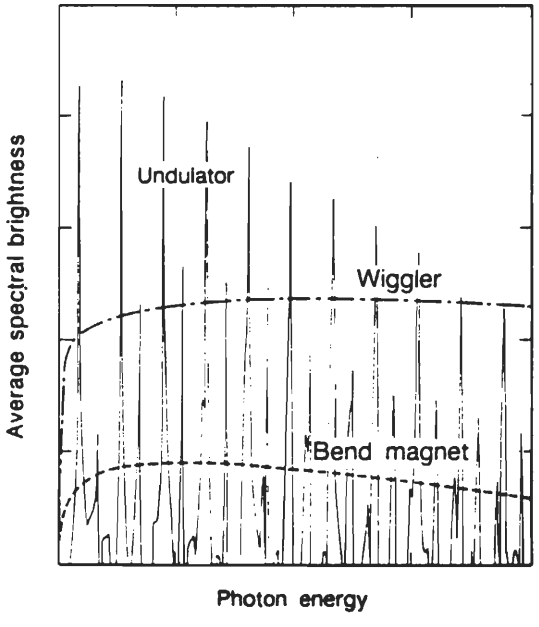

Figure 5. Comparison of output from "bending magnets," "wigglers," and "undulators." It can be seen that both the wiggler and bending magnets produce photons with a broad bandwidth, while the undulator delivers narrow bandwidth photons of high spectral brightness. This figure is reproduced from reference [33].

Another important feature of synchrotron radiation is the ability to select a monoenergetic (monochromatic) beam of photons. This is achieved by selecting a "slice" of the spectrum which emerges from the insertion devices. For the wavelengths used in this work, this monochromatization is achieved using a diffraction grating. When the incident broad-band beam reflects off of the diffraction grating at a grazing incidence, it is spatially dispersed by wavelength. A narrow slit can then move with respect to the dispersed beam and select the wavelength portion of beam desired. Furthermore, the slit width will determine the resolution of the beam. For a specific application, there is a trade-off between very narrow slit spacing (corresponding to high resolution with decreased flux) and wider slit spacing (corresponding to high flux with decreased resolution). In some cases, the slits are stationary and the grating is spherically curved. By rotating the grating with respect to the light, the dispersed beam then moves relative to the fixed slits, thereby only transmitting the desired wavelengths.

The measurements in this study were performed using the 8-cm-55-period U8 undulator of beamline 9.0.1 of the third generation Advanced Light Source of Lawrence Berkeley National Laboratory. The monochromatization was achieved using a spherical grating monochromater, and the exit slits were movable with respect to the grating. The photon resolution in the energy region of interest was measured to be approximately 110 meV (approximately 0.05%).

2. Time-of-flight spectroscopy

The electron spectra were collected using the experimental technique of time-of-flight spectrometry. With the synchrotron operating under double bunch operation, the source delivered two pulses of photons for every period of electron revolution in the storage ring. When the bunch impinges upon the gas target, the fastest electrons arrive at the detection plates and trigger the electronics to begin counting. As the remaining electrons travel to the detector, their time of travel over a fixed distance allows their kinetic energy to be determined. As the next "bunch" of photons begins to approach the gas target, a pulse is sent from the storage ring triggering the electronics to reset and await the arrival of the next bunch of electrons. The arrival of the fastest electrons of the next bunch begins the cycle anew. As the detector measures the arrival times of the electrons, the signal passes through a time to amplitude converter (TAC) into a multichannel analyzer (MCA).

Time-of-flight spectroscopy offers several advantages. Most importantly, an entire photoelectron Auger spectrum can be measured at once so that all features within a certain kinetic energy window are recorded simultaneously. This removes many experimental artifacts that would otherwise have to be contended with when measuring a spectrum in small kinetic energy steps. Furthermore, since multiple peaks can be recorded simultaneously, TOF spectrometers have a high efficiency. Finally, random events such as electron multiplier dark noise is averaged over a large number of channels. One drawback inherent to TOF spectrometry, though, is the non-linearity of the energy scale and the consequent decrease of spectrometer resolution at higher kinetic energies [36]. These disadvantages, however, exhibit only a small influence on the data. To try and overcome these inherent drawbacks, retardation voltages are used to increase the resolution of the high kinetic energy electrons.

3. Experimental setup

Two time-of-flight spectrometers are mounted to a rotatable vacuum chamber in a plane perpendicular to the photon beam. While measuring simultaneously at two angles with TOF spectrometers, it is possible to measure two complete spectra at once, thereby greatly reducing random errors generated by fluctuating conditions in such parameters as gas pressure or photon flux. As shown in Figure 6, the spectrometers were mounted at 0 degrees and 54.7 degrees with respect to the photon beam's electric field vector. The spectrometers are fixed to the rotatable chamber which rotates about the photon beam axis. A turbo pump was mounted directly to the chamber, while two additional turbo pumps were mounted to the spectrometers themselves.

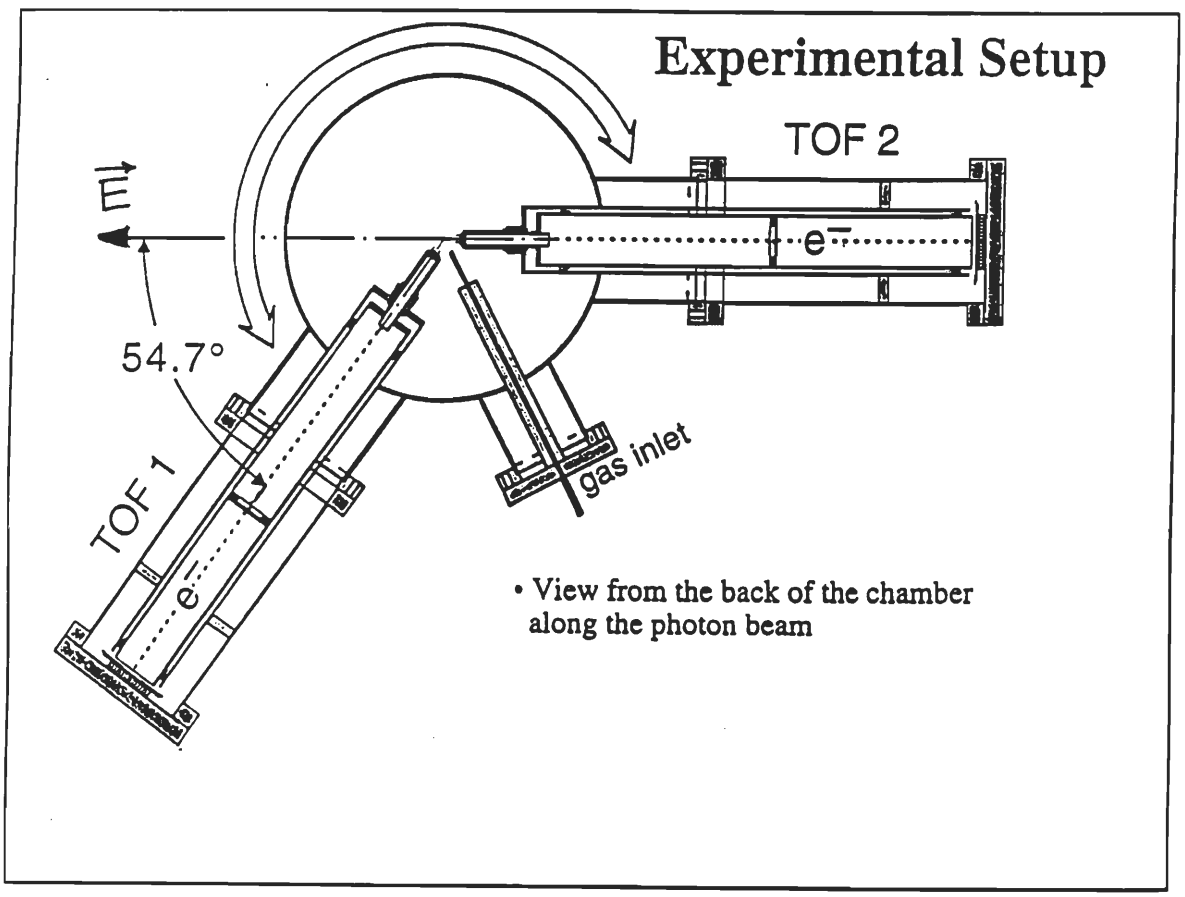

Figure 6. Schematic of the experimental setup. Two TOF spectrometers are mounted to a rotatable vacuum chamber in a plane perpendicular to the photon beam (the beam travels into the page).

Each TOF analyzer consists of a pair of microchannel plates and an anode detector plate mounted at the end of a 678.8 mm flight path. Figure 7 shows a schematic of a TOF spectrometer. To increase the resolution of the spectra in the kinetic region of interest, a 201 V retarding potential was applied to the flight tube, thus increasing the flight time of the electrons. The base pressure of the chamber was 3 x 10^{-8} Torr which ultimately rose to approximately 3 x 10^{-5} Torr as Ar gas was leaked in through a gas needle.

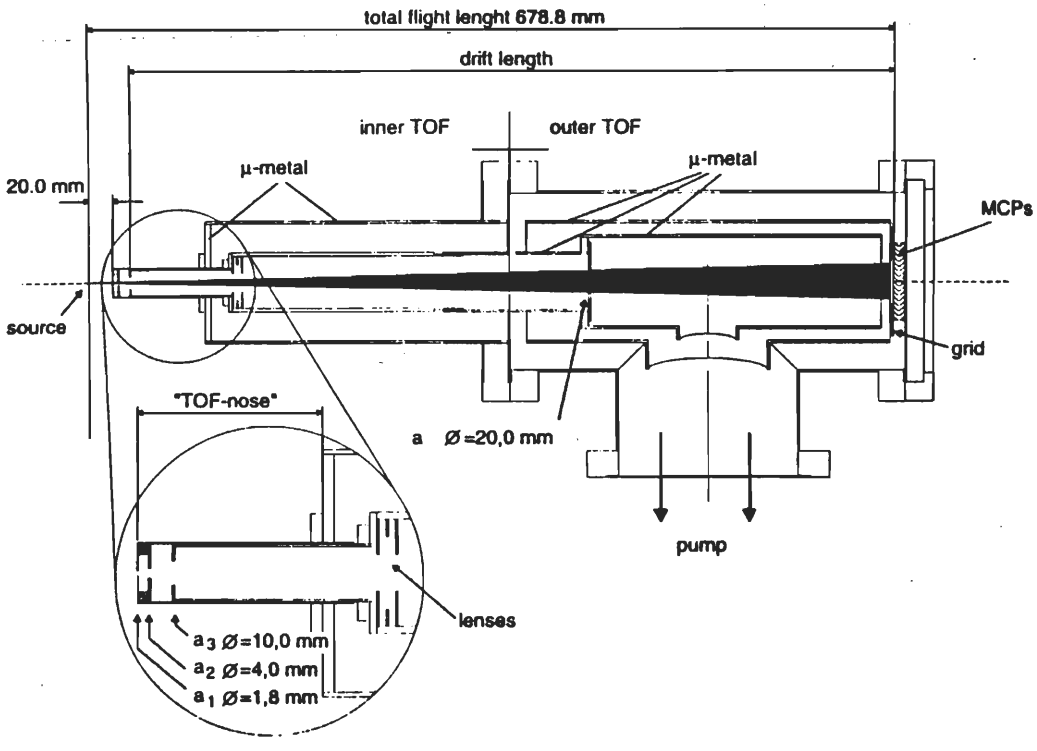

Figure 7. Schematic of a TOF spectrometer. At the end of the 678.8 mm drift length were mounted a pair of microchannel plates and an anode. To increase the detector resolution, a retarding potential was applied at the flight tube of the spectrometer, and a layer of magnetic shielding (μ-metal) was installed.

4. Data collection and analysis

To find the resonant photon energies for this study, an electron yield scan was taken in the ionization threshold region of the $2p_{3/2}$ and $2p_{1/2}$ shells. These ionization energies have been reported by King et. al. [37] as being 248.60 eV and 250.78 eV, respectively. The scan, which measured total electron yield (summed over both angles) versus photon energy, is shown in Figure 8. For each of the described measurements below, the absolute resonant energies reported have been quoted from King et. al. [37].

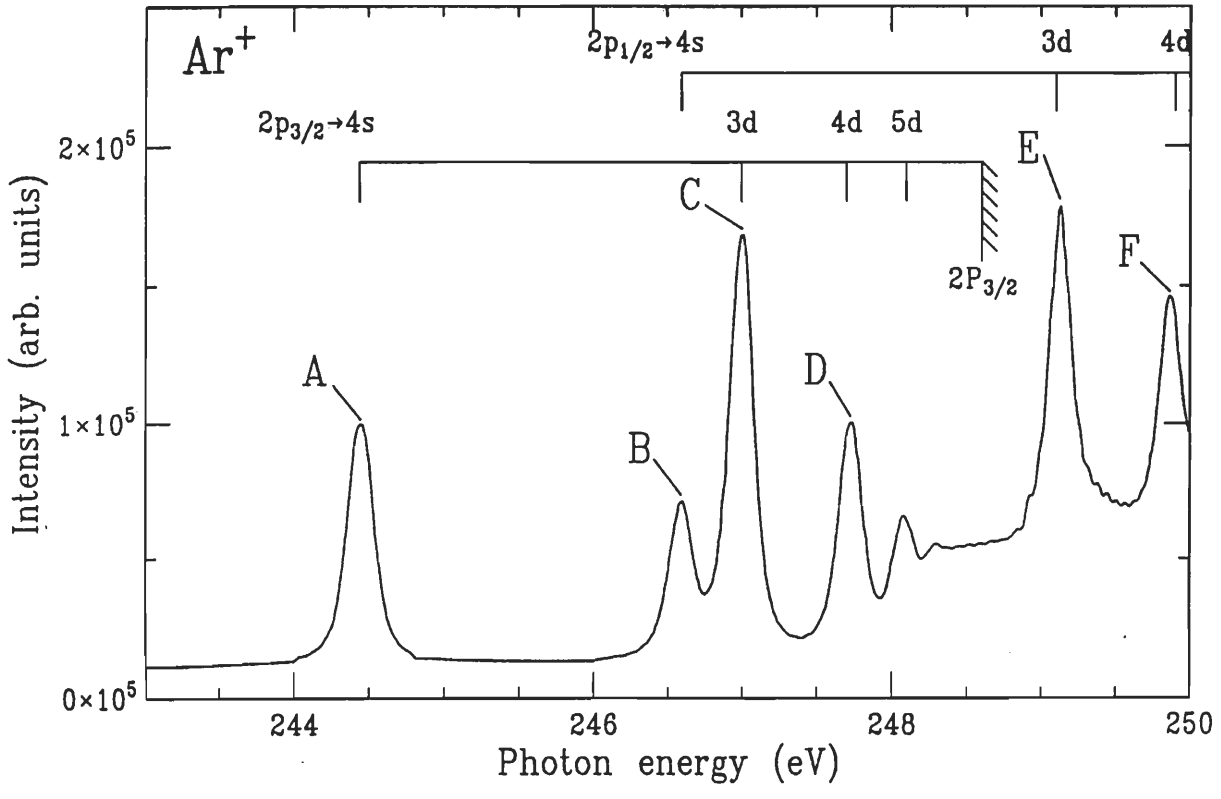

Figure 8. Photon energy scan over the $2p_{1/2,3/2}^{-1}4s$, $2p_{1/2,3/2}^{-1}3d$, and $2p_{1/2,3/2}^{-1}4d$ resonances. The vertical axis is total electron yield. These data were collected by making measurements at successive photon energy steps. From these data, the photon energy of each resonance was extracted, and these energies were then selected to record the kinetic energy spectra shown in Figure 9.

Operating at the photon energies determined by the scan, kinetic energy spectra were taken for each of the resonances. An average photon resolution of 107 meV was calculated for the specific photon energy and slit spacings used, and an average spectrometer resolution of 90 meV was determined from the measured linewidths (the measured width is a convolution of photon resolution and spectrometer resolution). These spectra were normalized to pressure and current, and a conversion from a time to a binding energy scale was then made. A plot of the six spectra considered in this study is shown in Figure 9 (here shown at the magic angle), and a discussion of

this plot is given in Chapter IV. The spectra were fit with Gaussian curves for each of the possible final ionic states remaining after the photoionization event. Since the only concern of this analysis was the correct identification of final states, the relative spacing of these final states was used to identify the peaks. This energy spacing was taken from the optical data of Minnhagen [38]. It was found that, as expected with TOF spectroscopy, the widths of these peaks increased slightly at higher kinetic energies, though not significant enough to interfere with this study. The end result of this portion of the analysis was a Gaussian fit to each identifiable final ionic state at each of the two angles.

From the areas of these curves, the angular distribution anisotropy parameter (β parameters) and relative intensity distributions could be extracted. The β parameter was calculated by substituting the areas of the curves at the two angles into equation 7. The relative intensity was calculated as the area of a specific peak divided by the sum of the peaks to which it was compared. (The reference peaks changed with each resonance). For each reported β parameter, an uncertainty was also reported which includes both a systematic error and a statistical error. The statistical uncertainty was calculated by applying the standard propagation of errors technique to equation 7 (see Bevington [39]) using the uncertainties in the fit parameters. The systematic uncertainty, which takes into account the sensitivity of the fit parameters, was found by performing a number of separate fits to a collection of overlapping peaks allowing for deviations in peak width and position. An error of 5% in area was found for strong, well-resolved peaks while an error of 10-20% in area was found for the weaker overlapping peaks. In every case, the appropriate systematic error was added to the statistical error, and this total uncertainty is given in parentheses after each reported value below. The uncertainty of each relative intensity was likewise calculated and reported.

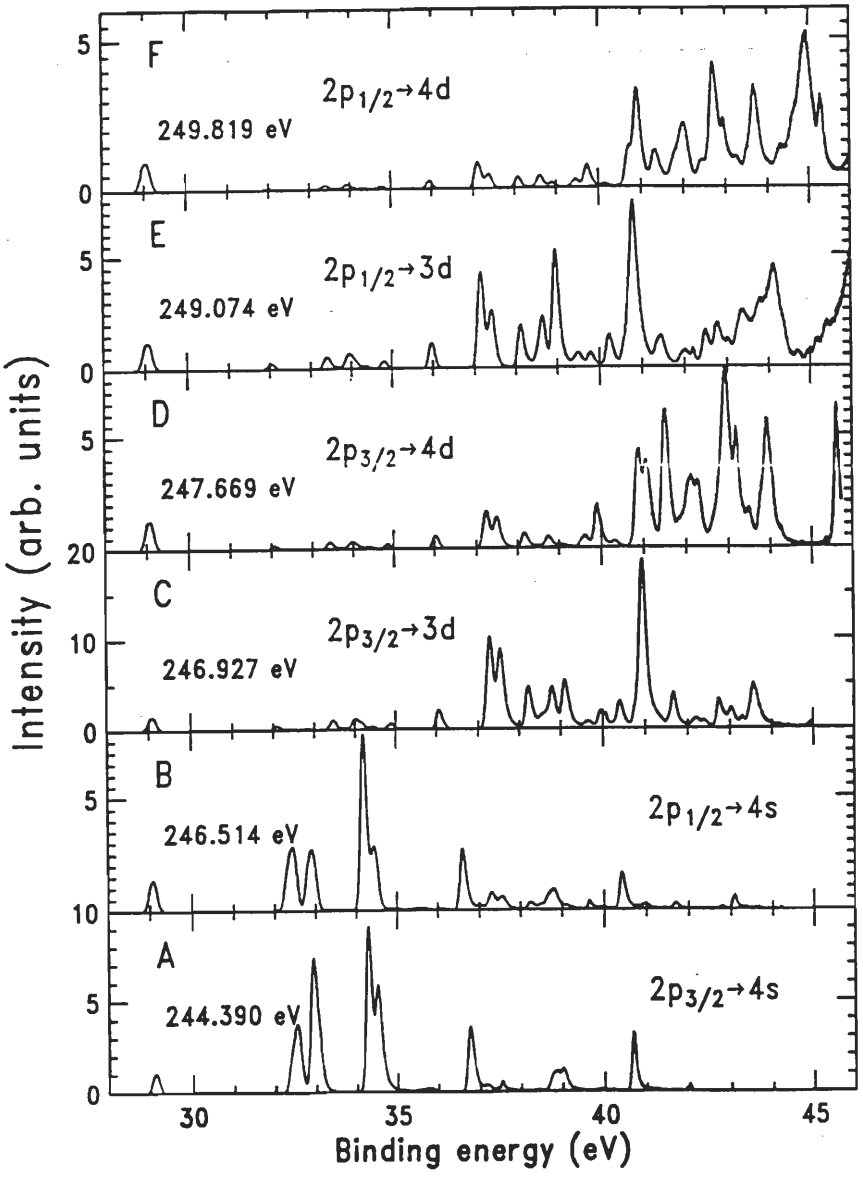

Figure 9. Kinetic energy spectra for the $2p_{1/2,3/2}^{-1}4s$ (B,A) $2p_{1/2,3/2}^{-1}3d$ (E,C) and $2p_{1/2,3/2}^{-1}4d$ (F,D) resonances. The photon energies used to make these measurements were taken from the photon energy scan shown in Figure 7. The accepted absolute resonant energies, taken from reference [37], are given in this figure. For each case, the intensity distribution is shown at the magic angle. The spectra were measured with a 201 V retarding potential applied to the flight tube.

IV. Results and discussion

1. The $2p^{-1}4s$ resonant Auger spectra

A plot of the $2p_{3/2}^{-1}4s$ and $2p_{1/2}^{-1}4s$ resonances are shown in Figures 9-A,B (measured at the magic angle). A comparison of these resonant Auger spectra with a normal non-resonant Auger spectra, shown in Figure 10, shows that as predicted by the spectator model, the resonant Auger spectrum looks much like the normal Auger spectrum with only a slight energy shift (due to the screening effect of the spectator electron). This result supports the validity of the spectator model for predicting relative intensities [13].

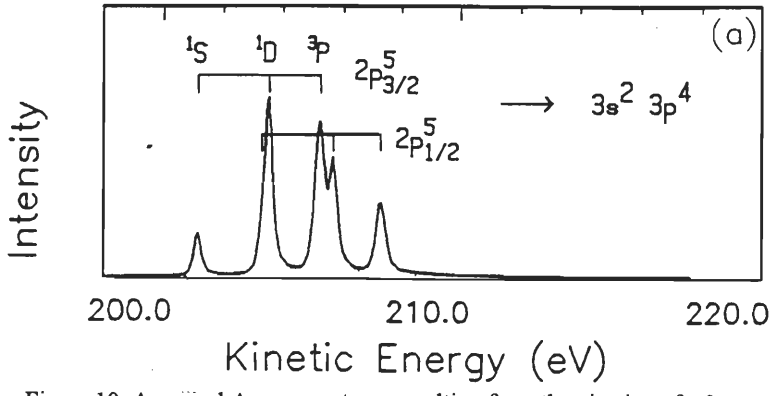

Figure 10. A normal Auger spectrum resulting from the ejection of a 2p electron in Ar. This figure was reproduced from reference [13].

Figures 11 and 12 depict portions of the $2p_{3/2}^{-1}4s$ and $2p_{1/2}^{-1}4s$ spectra, respectively. Each of the prominent features is labeled with a number, and each individual LS term is labeled by a numbered letter. Here, the same binding energy region is viewed from two different angles (0° and 54.7° with respect to the light's electric field). For each resolved final ionic state, a Gaussian peak has been fit with the relative spacing between the peaks assigned using optical data of Minnhagen [38]. Once the data from each spectrometer has been normalized to the spectrometers' relative efficiency (to compensate for transmission differences between them), a comparison of the areas of a particular peak at the two angles allows the β parameter to be determined using equation 7. These values are plotted in Figure 11-c and 12-c for the peaks in the displayed region. It can be observed from Figures 11-b and 12-b (note the different scales) that the relative populations of the final ionic states (viewed at different angles) are significantly different for the two different spin sublevels, although the β parameter for each final state is approximately the same.

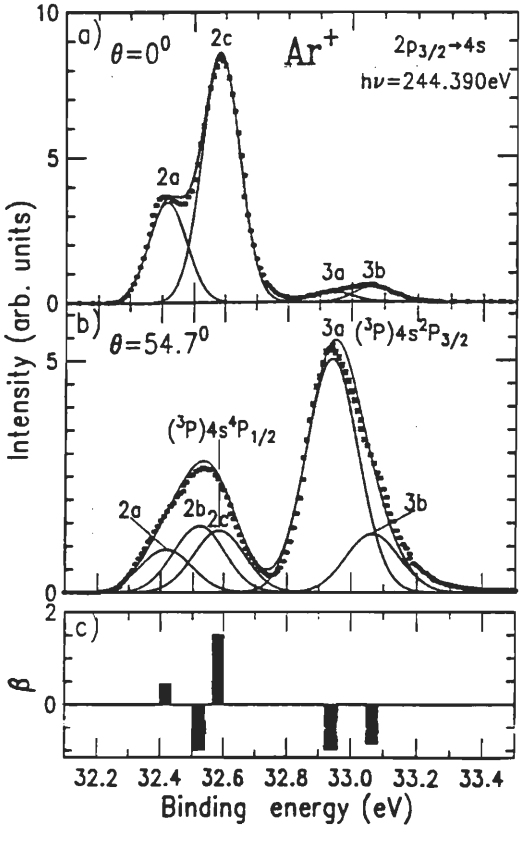

Figure 11. Auger decay spectra for the Ar $2p_{3/2}^{-1}4s$ resonance at (a) $\theta = 0°$ and (b) $\theta = 54.7°$. The peak labels correspond to those listed in Table 1. The angular distribution anisotropy parameters for the displayed states are shown in (c). These spectra were recorded with a 201 V retarding potential applied to the flight tube. The absolute resonant energies have been given by reference [37].

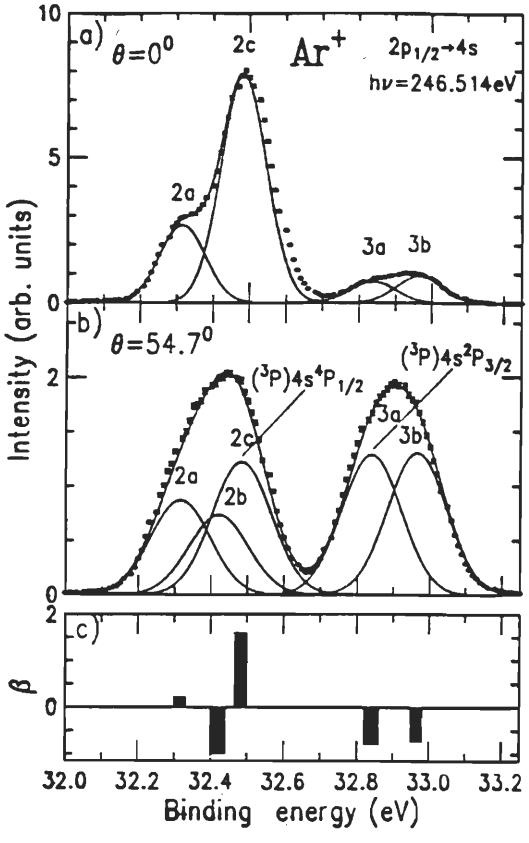

Figure 12. Auger decay spectra for the Ar $2p_{1/2}^{-1}4s$ resonance at (a) $\theta = 0°$ and (b) $\theta = 54.7°$. The peak labels correspond to those listed in Table 2. The angular distribution anisotropy parameters for the displayed states are shown in (c). These spectra were recorded with a 201 V retarding potential applied to the flight tube. The absolute resonant energies have been given by reference [37].

A complete listing of β parameters for nearly all $3p^4nl$ final ionic states is given in Table 1 for the $2p_{3/2}^{-1}4s$ decays and Table 2 for the $2p_{1/2}^{-1}4s$ decays. In order to compare these results with previously unresolved work, the individual β values for each j-level, and the average β value for the entire LS term (which includes the sum over all j-level peaks in a given LS term), are listed in all tables. For each value, the uncertainty is given in parentheses. The method of calculating uncertainties is described above in Chapter III, Section 4.

Final State $3p^4nl$		β Parameters : $2p_{3/2} \rightarrow 4s$					
		Experiment			*Theory*		
No	LS-term	β This work	β Carlson[22]	β Menzel[41]	β Hergenhahn[10]	β Chen[12]	β Cooper[9]
2a	$3p^4(^3P)4s^4P_{5/2}$	0.45(.06)				0.25	
2b	$3p^4(^3P)4s^4P_{3/2}$	-1.00(.05)				-0.88	
2c	$3p^4(^3P)4s^4P_{1/2}$	1.51(.13)				1.65	
2a,b,c	**$3p^4(^3P)4s^4P_{5/2,3/2,1/2}$**	**0.32(.05)**	**0.37**	**0.30**	**0.53**	**0.34**	**0.88**
3a	$3p^4(^3P)4s^2P_{3/2}$	-1.00(.05)				-0.98	
3b	$3p^4(^3P)4s^2P_{1/2}$	-0.85(.05)				-0.87	
3a,b	**$3p^4(^3P)4s^2P_{3/2,1/2}$**	**-0.94(.06)**	**-0.86**	**-0.93**	**-0.94**	**-0.95**	**-0.83**
2a,b,c	**$3p^4(^3P)4s^4P_{5/2,3/2,1/2}$**						
3a,b	**$3p^4(^3P)4s^2P_{3/2,1/2}$**	**-0.50(.03)**	**-0.65 -0.53**	**-0.47**	**-0.50**	**-0.47**	**-0.18**
7a	$3p^4(^1D)4s^2D_{3/2}$	0.66(.09)					
7b	$3p^4(^1D)4s^2D_{5/2}$	0.50(.06)					
8a	$3p^4(^3P)3d^2F_{7/2}$	*					
8b	$3p^4(^3P)3d^2F_{52}$	-0.35(.04)					
9a	$3p^4(^3P)3d^2D_{3/2}$	0.51(.06)					
9b	$3p^4(^3P)3d^2D_{5/2}$	0.55(.06)					
7a,b	**$3p^4(^1D)4s^2D_{5/2,3/2}$**						
8a,b	**$3p^4(^3P)3d^2F_{7/2,5/2}$**	**0.58(.07)**	**0.45 0.36**	**0.62**	**0.42**	**0.46**	**0.73**
9a,b	**$3p^4(^3P)3d^2D_{5/2,3/2}$**						
12a	$3p^4(^1S)4s^2S_{1/2}$	0.93(.09)	0.66 0.39	1.09	1.00	0.98	1.00

* Large positive β value.

Table 1. Experimental and theoretical angular distribution anisotropy parameters (β) for the Ar $2p_{3/2}^{-1}4s$ resonance. The uncertainty for each value is given in parentheses (see text for details). The resonant energy has been reported by reference [37] as 244.390 eV.

Final State $3p^4nl$		β Parameters : $2p_{1/2} \rightarrow 4s$					
		Experiment				*Theory*	
No	LS-term	β This work	β Carlson[22]	β Menzel[41]		β Hergenhahn[10]	β Chen[12]
2a	$3p^4(^3P)4s^4P_{5/2}$	0.21(.04)					0.19
2b	$3p^4(^3P)4s^4P_{3/2}$	-1.00(.05)					-0.81
2c	$3p^4(^3P)4s^4P_{1/2}$	1.61(.15)					1.8
2a,b,c	**$3p^4(^3P)4s^4P_{5/2,3/2,1/2}$**	**0.54(.07)**	**0.1**	**0.56**	**0.69**	**-**	**0.62**
3a	$3p^4(^3P)4s^2P_{3/2}$	-0.79(.04)					-0.79
3b	$3p^4(^3P)4s^2P_{1/2}$	-0.73(.04)					-0.72
3a,b	**$3p^4(^3P)4s^2P_{3/2,1/2}$**	**-0.75(.04)**	**-0.37**	**-0.57**	**-0.66**	**-**	**-0.75**
2a,b,c	**$3p^4(^3P)4s^4P_{5/2,3/2,1/2}$**						
3a,b	**$3p^4(^3P)4s^2P_{3/2,1/2}$**	**-0.09(.02)**	**-0.17**	**0.01**	**0.01**	**0.00**	**-0.007**
7a	$3p^4(^1D)4s^2D_{3/2}$	-1.00(.05)					
7b	$3p^4(^1D)4s^2D_{5/2}$	0.05(.03)					
8a	$3p^4(^3P)3d^2F_{7/2}$	*					
8b	$3p^4(^3P)3d^2F_{5/2}$	-0.52(.03)					
9a	$3p^4(^3P)3d^2D_{3/2}$	-0.15(.03)					
9b	$3p^4(^3P)3d^2D_{5/2}$	-0.04(.02)					
7a,b	**$3p^4(^1D)4s^2D_{5/2,3/2}$**						
8a,b	**$3p^4(^3P)3d^2F_{7/2,5/2}$**	**-0.03(.02)**	**-0.22**	**0.01**	**0.00**	**0.00**	**0.006**
9a,b	**$3p^4(^3P)3d^2D_{5/2,3/2}$**						
12a	$3p^4(^1S)4s^2S_{1/2}$	0.07(.03)	-0.20	0.00	0.00	0.00	0.001

* Large positive β value.

Table 2. Experimental and theoretical angular distribution anisotropy parameters (β) for the Ar $2p_{1/2}^{-1}4s$ resonance. The uncertainty for each value is given in parentheses (see text for details). The resonant energy has been reported by reference [37] as 246.514 eV.

It can be seen that most β parameters are either small positive values or negative values. A small magnitude value represents isotropic emission of the Auger electron while a negative value indicates a preferred emission in the direction perpendicular to the electric field vector of the radiation. The appearance of negative β values represents an enhanced population of final ionic states which can be reached via parity unfavored transitions only through resonant Auger processes [40].

These results were compared with earlier experimental work of Carlson et. al. [22] and Menzel et. al. [41], and with theoretical calculations of Cooper [9], Hergenhahn et. al. [10], and Chen [12]. Cooper treated the Auger decay as a single step process, whereas Hergenhahn et. al. have treated the excitation and decay as two distinct steps using the spectator model. Chen used the multiconfiguration Dirac-Fock method with intermediate coupling and configuration interaction, also a two-step model. In general, these results differ considerably from previous experimental results of Carlson et. al, attributed mostly to the poor resolution in the earlier experiment. Good agreement, however, is seen between the averaged LS term β parameters and those of Menzel [41] who was also unable to resolve individual j-levels. When compared with calculations, fair agreement is seen with Cooper's work [9], while much better agreement is seen with the work of Hergenhahn et. al. [10] and Chen [12]. It should

therefore be noted that the β parameters agree best with the two-step process calculations. It can also be seen from Tables 1 and 2 that, as predicted by the spectator model, the combined anisotropy of the ^2P and ^4P states is very close to zero for the $2p_{1/2}^{-1}4s$ resonance and to -0.5 in the case of the $2p_{3/2}^{-1}4s$ resonance, further supporting the spectator model.

Final State $3p^4nl$		Relative Intensities : $2p_{3/2} \rightarrow 4s$								
		Experiment				*Theory*				
No	LS-term	I(θ) This work	I(θ) Carlson[22]	I(θ) Menzel[41]	I(θ) Meyer[13]	I(θ) Chen[12]	I(θ) Hergenhahn[10]	I(θ) Cooper[9]	I(θ) Meyer[13,43]	
2a	$3p^4(^3P)4s^4P_{5/2}$	9.2(1.1)				12				
2b	$3p^4(^3P)4s^4P_{3/2}$	14.3(1.8)				12				
2c	$3p^4(^3P)4s^4P_{1/2}$	13.4(1.6)				13				
2a,b,c	**$3p^4(^3P)4s^4P_{5/2,3/2,1/2}$**	**36.9(2.3)**	**17**	**38**	**31**	**37**	**30**	**38**	**36**	**36**
3a	$3p^4(^3P)4s^2P_{3/2}$	50.4(2.8)				48				
3b	$3p^4(^3P)4s^2P_{1/2}$	12.7(1.6)				15				
3a,b	**$3p^4(^3P)4s^2P_{3/2,1/2}$**	**63.1(3.5)**	**83**	**62**	**69**	**63**	**70**	**62**	**64**	**64**
2a,b,c	**$3p^4(^3P)4s^4P_{5/2,3/2,1/2}$**									
3a,b	**$3p^4(^3P)4s^2P_{3/2,1/2}$**	**100.0**	**100**	**100**	**100**	**100**	**100**	**100**	**100**	
7a	$3p^4(^1D)4s^2D_{3/2}$	5.4(1.6)								
7b	$3p^4(^1D)4s^2D_{5/2}$	46.4(2.6)								
8a	$3p^4(^3P)3d^2F_{7/2}$	0.5(*)								
8b	$3p^4(^3P)3d^2F_{52}$	13.2(1.7)								
9a	$3p^4(^3P)3d^2D_{3/2}$	20.3(1.3)								
9b	$3p^4(^3P)3d^2D_{5/2}$	10.7(1.4)								
7a,b	**$3p^4(^1D)4s^2D_{5/2,3/2}$**									
8a,b	**$3p^4(^3P)3d^2F_{7/2,5/2}$**	**96.5(5.6)**	**86**	**119**	**108**	**110**	**75**	**75**	**78**	**80**	**46**
9a,b	**$3p^4(^3P)3d^2D_{5/2,3/2}$**									
12a	$3p^4(^1S)4s^2S_{1/2}$	21.0(1.2)	31	33	29	29	16	19	19	20	18

* Very weak line with large uncertainty.

Table 3. Experimental and theoretical relative intensities for the Ar $2p_{3/2}^{-1}4s$ resonance (measured at the magic angle). The uncertainty for each value is given in parentheses (see text for details). The resonant photon energy has been reported by reference [37] as 244.390 eV.

A listing of the relative intensities for the various final ionic states is given in Table 3 for the $2p_{3/2}^{-1}4s$ resonance and in Table 4 for the $2p_{1/2}^{-1}4s$ resonance, both showing comparisons to previous experimental and theoretical results. For both transitions, the relative intensities are taken with respect to the sum of the areas of the $(^3P)4s(^{4,2}P)$ peaks since these lines were well separated and did not overlap with other states. The uncertainty for each relative intensity has been displayed in parentheses following the value. These were calculated using the method described in Chapter III, Section 4. In this work, many final ionic states have been resolved that were not in any previous work.

Final State $3p^4nl$		Relative Intensities : $2p_{1/2} \rightarrow 4s$							
		Experiment					*Theory*		
No	LS-term	I(θ) This work	I(θ) Carlson[22]	I(θ) Menzel[41]		I(θ) Meyer[13]	I(θ) Chen[12]	I(θ) Meyer[13,43]	
2a	$3p^4(^3P)4s^4P_{5/2}$	16.1(2.0)					20		
2b	$3p^4(^3P)4s^4P_{3/2}$	13.6(1.9)					12		
2c	$3p^4(^3P)4s^4P_{1/2}$	22.5(1.6)					22		
2a,b,c	**$3p^4(^3P)4s^4P_{5/2,3/2,1/2}$**	**52.2(3.4)**	**42**	**51**	**51**	**50**	**54**	**54**	**55**
3a	$3p^4(^3P)4s^2P_{3/2}$	23.6(1.5)					23		
3b	$3p^4(^3P)4s^2P_{1/2}$	24.2(1.5)					23		
3a,b	**$3p^4(^3P)4s^2P_{3/2,1/2}$**	**47.8(2.8)**	**58**	**49**	**49**	**50**	**46**	**46**	**45**
2a,b,c	**$3p^4(^3P)4s^4P_{5/2,3/2,1/2}$**								
3a,b	**$3p^4(^3P)4s^2P_{3/2,1/2}$**	**100.0**	**100**	**100**		**100**	**100**	**100**	
7a	$3p^4(^1D)4s^2D_{3/2}$	19.2(1.7)							
7b	$3p^4(^1D)4s^2D_{5/2}$	69.7(4.3)							
8a	$3p^4(^3P)3d^2F_{7/2}$	0.9(*)							
8b	$3p^4(^3P)3d^2F_{5/2}$	15.3(2.0)							
9a	$3p^4(^3P)3d^2D_{3/2}$	10.1(1.6)							
9b	$3p^4(^3P)3d^2D_{5/2}$	20.3(1.4)							
7a,b	**$3p^4(^1D)4s^2D_{5/2,3/2}$**								
8a,b	**$3p^4(^3P)3d^2F_{7/2,5/2}$**	**135.5(8.6)**	**95**	**128**	**130**	**139**	**81**	**93**	**50**
9a,b	**$3p^4(^3P)3d^2D_{5/2,3/2}$**								
12a	$3p^4(^1S)4s^2S_{1/2}$	31.0(1.8)				24	29	24	23

* Approximately = 1.

Table 4. Experimental and theoretical relative intensities for the Ar $2p_{1/2}^{-1}4s$ resonance (measured at the magic angle). The uncertainty for each value is given in parentheses (see text for details). The resonant photon energy has been reported by reference [37] as 246.514 eV.

From these results it can be seen that the spectator model (Hergenhahn et. al. [10]), while predicting rather well the β parameters, does not predict the relative intensities as accurately as the model of Chen [12], which exhibits good agreement also with the measured β parameters. This may be due to the fact that Chen's model [12] calculates the full state vector and considers mixing of all the states, both important to determine the intensities. The spectator model, on the other hand, uses simple assumptions by relating the resonant and non-resonant Auger spectra and uses a smaller basis of state vectors [10]. This deficiency, however, does not affect the calculated β values significantly since this is a relative quantity describing the character of a certain transition independent of its strength [42]. The utility of the spectator model is its ability to give a simple physical explanation for the differences in the angular distribution of resonant and non-resonant Auger electrons [42].

2. The $2p^{-1}3d$ resonant Auger spectra

The complete $2p_{3/2}^{-1}3d$ and $2p_{1/2}^{-1}3d$ spectra are given in Figures 9-C,E (measured at the magic angle). Contrary to the $2p^{-1}4s$ case described above, the spectator model is less successful for predicting the relative intensities of the $2p^{-1}3d$ resonances, i.e. the observed spectra are much different from the normal non-resonant spectra (Figure 10 [13]). Instead, the spectra are dominated by shake up processes. Reasons for this have been discussed by Aksela et. al. [21] and Mursu et. al. [24]. Another explanation has been provided by Meyer et. al. [13], who described in some detail the special properties of the wave function which leads to a high shake up probability.

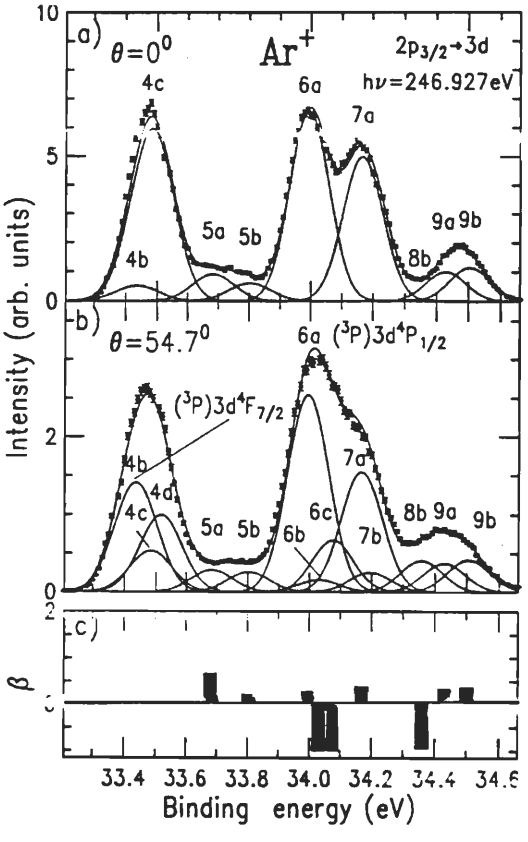

Figure 13. Auger decay spectra for the Ar $2p_{3/2}^{-1}3d$ resonance at (a) $\theta = 0°$ and (b) $\theta = 54.7°$. The peak labels correspond to those listed in Table 5. The angular distribution anisotropy parameters for the displayed states are shown in (c). These spectra were recorded with a 201 V retarding potential applied to the flight tube. The absolute resonant energies have been given by reference [37].

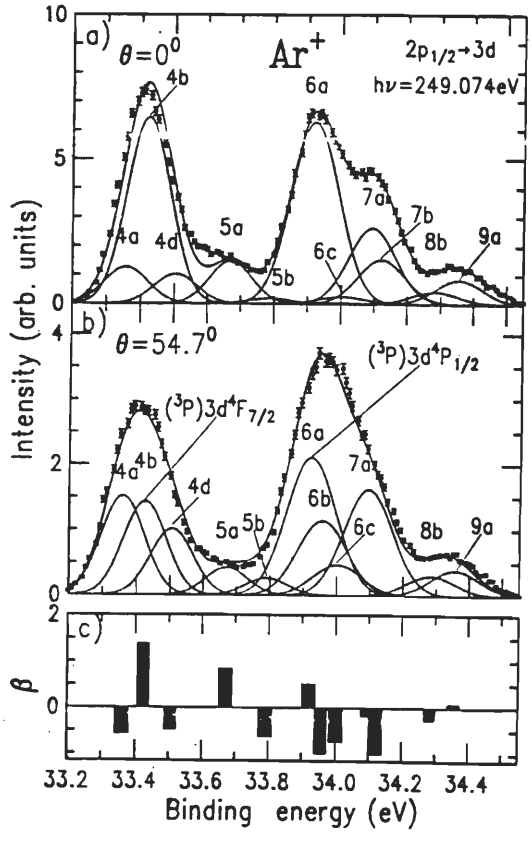

Figure 14. Auger decay spectra for the Ar $2p_{1/2}^{-1}3d$ resonance at (a) $\theta = 0°$ and (b) $\theta = 54.7°$. The peak labels correspond to those listed in Table 6. The angular distribution anisotropy parameters for the displayed states are shown in (c). These spectra were recorded with a 201 V retarding potential applied to the flight tube. The absolute resonant energies have been given by reference [37].

Figure 13 and 14 show smaller portions of the resonant Auger spectra of the $2p_{3/2}^{-1}3d$ and $2p_{1/2}^{-1}3d$ excitations, respectively. These figures demonstrate the large overlap of peaks which made the identification of the individual j-levels per LS term difficult. If a peak is not well resolved, the fit parameters will have a larger uncertainty, ultimately leading to a larger uncertainty in the relative intensities and β parameters. After applying the same fitting procedure described for the $2p^{-1}4s$ resonance above, the relative intensities and β parameters were extracted for the various final ionic states. A complete listing of these values is provided by Tables 5 and 6, and a comparison to the experimental relative intensities of Mursu et. al. [24] has been made. In these tables, the uncertainty for each β parameter and relative intensity is given in parentheses following the value. These uncertainties were calculated as described in Chapter III, Section 4. For these transitions, the relative intensities have been normalized with respect to the area of the $(^1D)3d(^2F_{5/2,7/2})$ state. The data of Mursu et. al. [24] have been converted to match this normalization in order to facilitate comparison. The discrepancies between these results and those of Mursu et. al. [24] for the relative intensities of closely spaced peaks can be explained by the difficulty in resolving the overlapping peaks in both sets of data, as mentioned above. Hence, the relative intensities of neighboring peaks must be considered as estimates only. In all cases, all overlapping individual j-levels (e.g. $3d^4D_{7/2,5/2,3/2,1/2}$) within an LS term ($3d^4D$) were combined under the LS term, and this value is shown in bold. A comparison or each complete LS term shows overall good agreement with the previous data.

Final State $3p^4nl$			Relative Intensity : $2p_{3/2} \rightarrow 3d$		β Parameters : $2p_{3/2} \rightarrow 3d$
No		LS-term	I (θ) This work	$I(\theta)$[24]	β This work
1a	32.077	$3p^4(^3P)3d^4D_{7/2}$	5.4(1.7)	9.6	-1.00(.10)
1b	32.096	$3p^4(^3P)3d^4D_{5/2}$	7.1(1.8)	5.7	0.67(.07)
1c	32.115	$3p^4(^3P)3d^4D_{3/2}$	12.2(1.6)	3.9	-0.38(.03)
1d	32.128	$3p^4(^3P)3d^4D_{1/2}$	-	12.2	-
1a,b,c,d		**$3p^4(^3P)3d^4D_{7/2,5/2,3/2,1/2}$**	**24.7(2.0)**	**31.4**	**-0.16(.03)**
2a	32.315	$3p^4(^3P)4s^4P_{5/2}$	-	-	-
2b	32.420	$3p^4(^3P)4s^4P_{3/2}$	5.1(1.3)	3.5	-1.00(.10)
2c	32.483	$3p^4(^3P)4s^4P_{1/2}$	0.7(0.5)	7.3	2.00(.20)
2a,b,c		**$3p^4(^3P)4s^4P_{5/2,3/2,1/2}$**	**5.8(1.7)**	**10.8**	**-0.12(.03)**
4a	33.370	$3p^4(^3P)3d^4F_{9/2}$	-	-	-
4b	33.436	$3p^4(^3P)3d^4F_{7/2}$	25.8(1.8)	-	-0.82(.05)
4c	33.484	$3p^4(^3P)3d^4F_{5/2}$	9.8(2.3)	41.7	*
4d	33.517	$3p^4(^3P)3d^4F_{3/2}$	18.2(2.3)	23.5	-1.00(.05)
4a,b,c,d		**$3p^4(^3P)3d^4F_{9/2,7/2,5/2,3/2}$**	**53.8(4.2)**	**65.2**	**0.07(.01)**
5a	33.683	$3p^4(^3P)3d^2P_{1/2}$	5.2(1.4)	-	0.67(.09)
5b	33.802	$3p^4(^3P)3d^2P_{3/2}$	4.8(1.3)	7.8	0.23(.05)
5a,b		**$3p^4(^3P)3d^2P_{3/2,1/2}$**	**10.0(1.5)**	**7.8**	**0.43(.06)**
6a	33.995	$3p^4(^3P)3d^4P_{1/2}$	45.3(2.9)	30.4	0.29(.04)
6b	34.029	$3p^4(^3P)3d^4P_{3/2}$	2.8(1.5)	32.6	-1.00(.10)
6c	34.075	$3p^4(^3P)3d^4P_{5/2}$	11.9(1.9)	-	-1.00 (.05)
6a,b,c		**$3p^4(^3P)3d^4P_{5/2,3/2,1/2}$**	**60.0(4.4)**	**63.0**	**-0.03(.02)**
7a	34.167	$3p^4(^1D)4s^2D_{3/2}$	27.5(1.9)	39.1	0.62(.09)
7b	34.195	$3p^4(^1D)4s^2D_{5/2}$	4.5(1.8)	-	-1.00(.10)
7a,b		**$3p^4(^1D)4s^2D_{5/2,3/2}$**	**32.0(2.6)**	**39.1**	**0.39(.06)**
8a	34.237	$3p^4(^3P)3d^2F_{7/2}$	-	-	-
8b	34.357	$3p^4(^3P)3d^2F_{5/2}$	7.2(1.8)	-	-0.95(.10)
8a,b		**$3p^4(^3P)3d^2F_{7/2,5/2}$**	**7.2(1.8)**	**-**	**-0.54(.07)**
9a	34.429	$3p^4(^3P)3d^2D_{3/2}$	6.6(1.9)	12.6	0.35(.06)
9b	34.509	$3p^4(^3P)3d^2D_{5/2}$	7.4(1.8)	10.43	0.38(.07)
9a,b		**$3p^4(^3P)3d^2D_{5/2,3/2}$**	**14.0(2.1)**	**23.03**	**0.37(.05)**
10a	34.888	$3p^4(^1D)3d^2G_{9/2}$	31.4(2.0)	43.5	-0.10(.02)
10b	34.891	$3p^4(^1D)3d^2G_{7/2}$	-	-	-
10a,b		**$3p^4(^1D)3d^2G_{9/2,7/2}$**	**45.4(2.8)**	**66.53**	**0.24(.04)**
11a	36.059	$3p^4(^1D)3d^2F_{5/2}$	25.1(1.8)	100.0	0.31(.04)
11b	36.085	$3p^4(^1D)3d^2F_{7/2}$	74.9(4.3)	-	-0.29(.03)
11a,b		**$3p^4(^1D)3d^2F_{7/2,5/2}$**	**100.0**	**100.0**	**-0.14(.03)**
13a	37.270	$3p^4(^1D)3d^2D_{5/2}$	294(16)	260.0	0.26(.04)
13b	37.331	$3p^4(^1D)3d^2D_{3/2}$	225(13)	285.0	0.13(.04)
13a,b		**$3p^4(^1D)3d^2D_{5/2,3/2}$**	**519(28)**	**545.0**	**0.20(.04)**
14a	37.527	$3p^4(^1D)3d^2P_{3/2}$	242(13)	220.0	-0.98(.06)
14b	37.578	$3p^4(^1D)3d^2P_{1/2}$	191(11)	185.0	-0.64(.04)
14a,b		**$3p^4(^1D)3d^2P_{3/2,1/2}$**	**434(23)**	**405.0**	**-0.83(.05)**
15a	38.212	$3p^4(^1S)3d^2D_{5/2}$	127(7)	168.0	-0.01(.02)
15b	38.254	$3p^4(^1S)3d^2D_{3/2}$	98.8(6.0)	74.0	-0.01(.02)
15a.b		**$3p^4(^1S)3d^2D_{5/2,3/2}$**	**226(13)**	**242.0**	**-0.01(.02)**
19	38.645	$3p^4(^1D)3d^2S_{1/2}$	168.0(9.2)	146.0	0.16(.04)

* Large positive β value.

Table 5. Experimental relative intensities (measured at the magic angle) and β parameters for the Ar $2p_{3/2}^{-1}3d$ resonance. The uncertainties of the intensities and of the β parameters are given in parentheses. The resonant energy has been reported by reference [37] as 246.927 eV. In addition to the values displayed for the individual j-levels, their averaged sum per LS term is shown in bold. See text for details.

Final State $3p^4nl$		Relative Intensity : $2p_{1/2} \rightarrow 3d$		β Parameters : $2p_{1/2} \rightarrow 3d$
No	LS-term	I (θ) This work	I (θ)[24]	β This work
1a	$3p^4(^3P)3d^4D_{7/2}$	25.2(1.7)	15.2	-0.10(.02)
1b	$3p^4(^3P)3d^4D_{5/2}$	0.1(**)	2.9	*
1c	$3p^4(^3P)3d^4D_{3/2}$	-	2.5	-
1d	$3p^4(^3P)3d^4D_{1/2}$	1.3(0.7)	11.5	*
1a,b,c,d	**$3p^4(^3P)3d^4D_{7/2,5/2,3/2,1/2}$**	**26.6(2.5)**	**32.1**	**0.03(.03)**
2a	$3p^4(^3P)4s^4P_{5/2}$	2.2(0.8)	3.3	0.48(.08)
2b	$3p^4(^3P)4s^4P_{3/2}$	2.4(0.7)	9.5	-0.70(.08)
2c	$3p^4(^3P)4s^4P_{1/2}$	0.1(0.4)	-	*
2a,b,c	**$3p^4(^3P)4s^4P_{5/2,3/2,1/2}$**	**4.7(1.5)**	**12.8**	**0.47(.08)**
4a	$3p^4(^3P)3d^4F_{9/2}$	21.3(1.5)	-	- 0.57(.03)
4b	$3p^4(^3P)3d^4F_{7/2}$	20.0(1.8)	-	1.39(.13)
4c	$3p^4(^3P)3d^4F_{5/2}$	-	38.3	-
4d	$3p^4(^3P)3d^4F_{3/2}$	14.2(1.9)	27.6	-0.48(.03)
4a,b,c,d	**$3p^4(^3P)3d^4F_{9/2,7/2,5/2,3/2}$**	**55.5(3.8)**	**65.9**	**0.11(.04)**
5a	$3p^4(^3P)3d^2P_{1/2}$	5.9(1.6)	4.1	0.84(.13)
5b	$3p^4(^3P)3d^2P_{3/2}$	3.7(1.1)	6.6	-0.63(.07)
5a,b	**$3p^4(^3P)3d^2P_{3/2,1/2}$**	**9.6(1.5)**	**10.7**	**0.29(.04)**
6a	$3p^4(^3P)3d^4P_{1/2}$	34.0(2.4)	15.6	0.51(.06)
6b	$3p^4(^3P)3d^4P_{3/2}$	18.3(1.5)	54.3	-1.00(.05)
6c	$3p^4(^3P)3d^4P_{5/2}$	7.5(2.1)	-	-0.74(.08)
6a,b,c	**$3p^4(^3P)3d^4P_{5/2,3/2,1/2}$**	**59.8(4.0)**	**69.9**	**-0.07(.02)**
7a	$3p^4(^1D)4s^2D_{3/2}$	26.0(2.0)	33.7	-0.19(.03)
7b	$3p^4(^1D)4s^2D_{5/2}$	0.1(0.1)	-	-1.00(.10)
7a,b	**$3p^4(^1D)4s^2D_{5/2,3/2}$**	**26.0(2.0)**	**33.7**	**0.28(.04)**
8a	$3p^4(^3P)3d^2F_{7/2}$	-	-	-
8b	$3p^4(^3P)3d^2F_{5/2}$	4.9(1.4)	-	-0.3(.05)
8a,b	**$3p^4(^3P)3d^2F_{7/2,5/2}$**	**4.9(1.4)**	**-**	**-0.3(.05)**
9a	$3p^4(^3P)3d^2D_{3/2}$	6.2(1.7)	9.5	0.09(.03)
9b	$3p^4(^3P)3d^2D_{5/2}$	0.3(0.3)	9.1	*
9a,b	**$3p^4(^3P)3d^2D_{5/2,3/2}$**	**6.5(1.9)**	**18.6**	**0.44(.08)**
10a	$3p^4(^1D)3d^2G_{9/2}$	17.1(2.2)	42.8	-1.00(.05)
10b	$3p^4(^1D)3d^2G_{7/2}$	12.5(1.7)	-	*
10a,b	**$3p^4(^1D)3d^2G_{9/2,7/2}$**	**29.6(2.1)**	**42.8**	**0.36(.05)**
11a	$3p^4(^1D)3d^2F_{5/2}$	71.5(4.2)	100.0	-0.25(.03)
11b	$3p^4(^1D)3d^2F_{7/2}$	28.5(2.5)	-	0.11(.03)
11a,b	**$3p^4(^1D)3d^2F_{7/2,5/2}$**	**100.0**	**100.0**	**-0.18(.03)**
13a	$3p^4(^1D)3d^2D_{5/2}$	254(13)	284.0	0.17(.04)
13b	$3p^4(^1D)3d^2D_{3/2}$	150.0(8.7)	124.0	-0.22(.03)
13a,b	**$3p^4(^1D)3d^2D_{5/2,3/2}$**	**404(22)**	**408.0**	**0.05(.02)**
14a	$3p^4(^1D)3d^2P_{3/2}$	124.0(7.1)	152.0	-1.00(.05)
14b	$3p^4(^1D)3d^2P_{1/2}$	117.0(6.6)	81.0	0.01(.02)
14a,b	**$3p^4(^1D)3d^2P_{3/2,1/2}$**	**241(13)**	**233.0**	**-0.49(.03)**
15a	$3p^4(^1S)3d^2D_{5/2}$	2.7(1.4)	14.0	*
15b	$3p^4(^1S)3d^2D_{3/2}$	161.0(8.9)	151.0	-0.39(.04)
15a.b	**$3p^4(^1S)3d^2D_{5/2,3/2}$**	**163.7(9.5)**	**165.0**	**-0.33(.03)**
19	$3p^4(^1D)3d^2S_{1/2}$	148.0(8.2)	138.0	0.84(.09)

* Large positive β value.

** Very weak line having large uncertainty.

Table 6. Experimental relative intensities (measured at the magic angle) and β parameters for the Ar $2p_{1/2}^{-1}3d$ resonance. The uncertainties of the intensities and of the β parameters are given in parentheses. The resonant energy has been reported by reference [37] as 249.074 eV. In addition to the values displayed for the individual j-levels, their averaged sum per LS term is shown in bold. See text for details.

These β parameters were first reported through this effort [32]. As seen in the $2p^{-1}4s$ resonances above, nearly all states demonstrate small positive or negative β parameters. Additionally, in nearly all cases, a comparison of the complete LS term's β parameter between the $2p_{3/2}^{-1}3d$ and $2p_{1/2}^{-1}3d$ resonance shows agreement for most cases.

3. The $2p^{-1}4d$ resonant Auger spectra

The complete photoelectron spectra for the $2p^{-1}4d$ resonances, measured at the magic angle, are shown in Figures 9-D,F. As evidenced by the dissimilarity between these resonant Auger spectra and the normal Auger spectra (Figure 10 [13]), the $2p^{-1}4d$ resonances likewise demonstrate a breakdown of the spectator model in predicting relative intensities. Reasons for this are cited above for the $2p^{-1}3d$ case, which states that this is due to strong shake up modifications as proposed by Aksela et. al. [21] and Mursu et. al. [24].

Figures 15 and 16 show portions of the $2p_{3/2}^{-1}4d$ and $2p_{1/2}^{-1}4d$ resonances, respectively. Here, the extracted β parameters for the peaks in this region are displayed in Figure 15-c and 16-c. The dominance of negative β parameters, corresponding to preferred electron emission perpendicular to the electric field, is again observed for these resonances. This supports Cooper's theory [9], which was only applied to the case of the $2p^{-1}4s$ resonances, but which seems to be also valid for the $2p^{-1}3d$ and $2p^{-1}4d$ resonances. The similarity of β values at the two different spin sublevel resonances ($2p_{3/2}^{-1}4d$ and $2p_{1/2}^{-1}4d$) is again seen here.

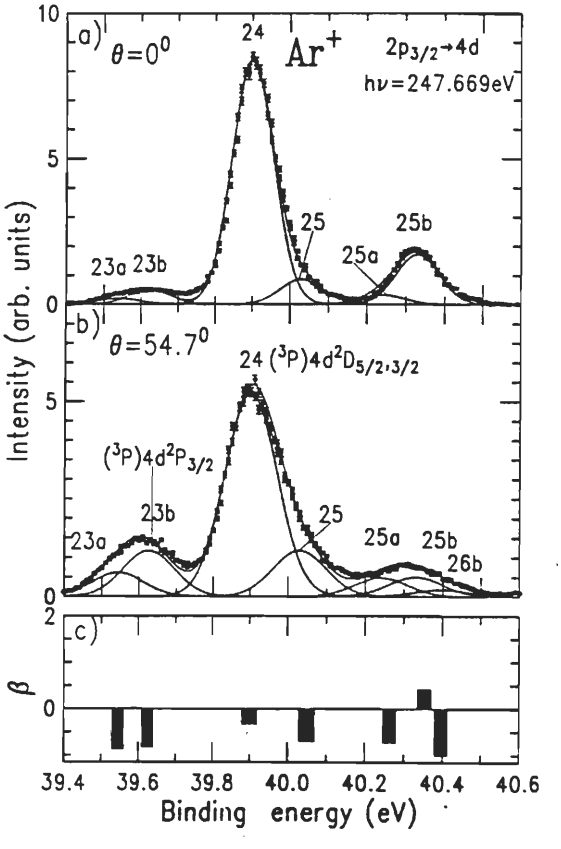

Figure 15. Auger decay spectra for the Ar $2p_{3/2}^{-1}4d$ resonance at (a) $\theta = 0°$ and (b) $\theta = 54.7°$. The peak labels correspond to those listed in Table 7. The angular distribution anisotropy parameters for the displayed states are shown in (c). These spectra were recorded with a 201 V retarding potential applied to the flight tube. The absolute resonant energies have been given by reference [37].

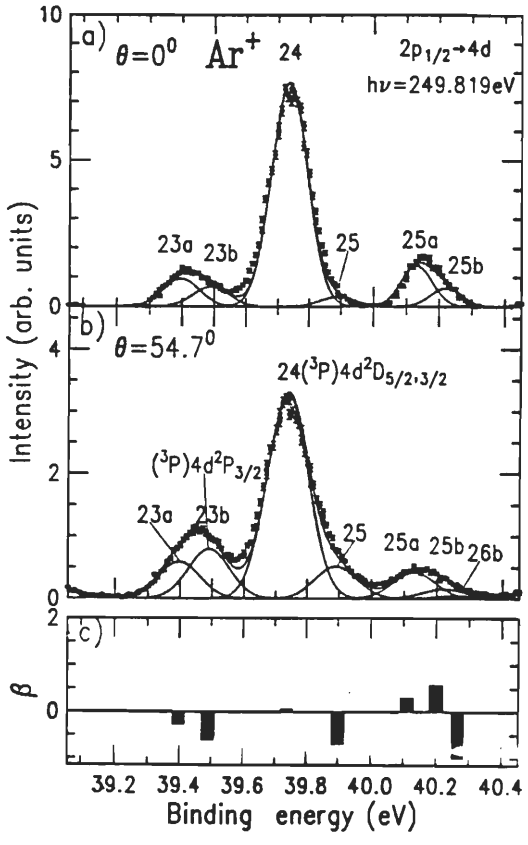

Figure 16. Auger decay spectra for the Ar $2p_{1/2}^{-1}4d$ resonance at (a) $\theta = 0°$ and (b) $\theta = 54.7°$. The peak labels correspond to those listed in Table 8. The angular distribution anisotropy parameters for the displayed states are shown in (c). These spectra were recorded with a 201 V retarding potential applied to the flight tube. The absolute resonant energies have been given by reference [37].

A complete listing of relative intensities and β parameters for most final ionic states is given in Tables 7-8. The uncertainty in each β parameter and relative intensity is displayed after each value. These uncertainties were calculated as described in Chapter III, Section 4. For this resonance, the relative intensities have been normalized with respect to the well-separated $(^3P)4d(^2P_{1/2,3/2})$ lines. The relative intensities of the $2p_{3/2}^{-1}4d$ peaks have been compared with those of Mursu et. al. [24], and those data have been converted to match this normalization. These are the first reported relative intensities for the $2p_{1/2}^{-1}4d$ resonance. As these are also the first angular resolved measurements for the $2p^{-1}4d$ resonances, the β parameters were reported with this effort for the first time [32].

Final State $3p^4nl$		Relative Intensity : $2p_{3/2} \rightarrow 4d$		β Parameters : $2p_{3/2} \rightarrow 4d$
No	LS-term	I (θ) This work	I (θ)[24]	β This work
15a	$3p^4(^1S)3d^2D_{5/2}$	83.9(5.0)	95.6	-0.68(.04)
15b	$3p^4(^1S)3d^2D_{3/2}$	31.9(2.7)	33.7	-0.50(.03)
15a,b	**$3p^4(^1S)3d^2D_{5/2,3/2}$**	**115.8(7.2)**	**129.3**	**-0.62(.04)**
16a	$3p^4(^3P)5s^4P_{5/2}$	15.8(2.1)	-	-0.93(.05)
16b	$3p^4(^3P)5s^4P_{3/2}$	2.8(1.5)	23.9	-0.81(.09)
16c	$3p^4(^3P)5s^4P_{1/2}$	6.6(1.9)	-	-0.90(.09)
16a,b,c	**$3p^4(^3P)5s^4P_{5/2,3/2,1/2}$**	**25.2(2.6)**	**23.9**	**-0.90(.05)**
17a	$3p^4(^3P)5s^2P_{3/2}$	-	-	-
18a	$3p^4(^3P)4d^4D_{7/2}$	-	-	-
18b	$3p^4(^3P)4d^4D_{5/2}$	-	-	-
17b	$3p^4(^3P)5s^2P_{1/2}$	-	-	-
17a,b	**$3p^4(^3P)5s^2P_{3/2,1/2}$**	**-**	**-**	**-**
18c	$3p^4(^3P)4d^4D_{3/2}$	50.1(3.5)	82.6	-0.06(.02)
19	$3p^4(^1D)3d^2S_{1/2}$	42.2(3.1)	56.5	0.84(.08)
18d	$3p^4(^3P)4d^4D_{1/2}$	-	-	-
18a,b,c,d	**$3p^4(^3P)4d^4D_{7/2,5/2,3/2,1/2}$**	**50.1(3.5)**	**82.6**	**-0.06(.02)**
20a	$3p^4(^3P)4d^4F_{9/2}$	1.4(**)	-	*
20b	$3p^4(^3P)4d^4F_{7/2}$	9.3(1.5)	15.2	-1.00(.05)
21a	$3p^4(^3P)4d^4P_{1/2}$	15.4(2.3)	-	-0.30(.05)
20c	$3p^4(^3P)4d^4F_{5/2}$	-	32.6	-
20a,b,c	**$3p^4(^3P)4d^4F_{9/2,7/2,5/2}$**	**10.7(2.6)**	**47.8**	**-0.95(.05)**
21b	$3p^4(^3P)4d^4P_{3/2}$	-	-	-
22a	$3p^4(^3P)4d^2F_{7/2}$	-	-	-
21c	$3p^4(^3P)4d^4P_{5/2}$	7.6(1.5)	10.8	-1.00(.05)
21a,b,c	**$3p^4(^3P)4d^4P_{5/2,3/2,1/2}$**	**23.0(1.9)**	**10.8**	**-0.53(.03)**
22b	$3p^4(^3P)4d^2F_{5/2}$	9.4(1.4)	-	-0.70(.04)
22a,b	**$3p^4(^3P)4d^2F_{7/2,5/2}$**	**9.4(1.4)**	**-**	**-0.70(.04)**
23a	$3p^4(^3P)4d^2P_{1/2}$	34.4(2.4)	46.7	-0.88(.05)
23b	$3p^4(^3P)4d^2P_{3/2}$	65.6(4.2)	53.3	-0.83(.05)
23a,b	**$3p^4(^3P)4d^2P_{3/2,1/2}$**	**100.0**	**100.0**	**-0.85(.05)**
24	$3p^4(^3P)4d^2D_{5/2,3/2}$	291(16)	330.4	-0.34(.03)
25	$3p^4(^3P)5s^2D_{5/2,3/2}$	65.6(4.1)	36.9	-0.71(.04)
25a	$3p^4(^1D)4d^2G_{9/2}$	26.7(1.9)	-	-0.73(.04)
25b	$3p^4(^1D)4d^2G_{7/2}$	28.2(2.4)	-	0.42(.06)
25a,b	**$3p^4(^1D)4d^2G_{9/2,7/2}$**	**54.9(3.9)**	**-**	**-0.15(.03)**
26a	$3p^4(^3P)6s^4P_{5/2}$	-	-	-
26b	$3p^4(^3P)6s^4P_{3/2,1/2}$	10.1(1.6)	-	-1.00(.05)
26a,b	**$3p^4(^3P)6s^4P_{5/2,3/2,1/2}$**	**10.1(1.6)**	**-**	**-1.00(.05)**
27	$3p^4(^1D)4d^2D_{5/2,3/2}$	292(17)	469.5	-0.35(.03)
28	$3p^4(^1D)4d^2P_{3/2,1/2}$	415(23)	131.5	-0.43(.03)

* Large positive β value.

** Very weak line having large uncertainty.

Table 7. Experimental relative intensities (measured at the magic angle) and β parameters for the Ar $2p_{3/2}^{-1}4d$ resonance. The uncertainties of the intensities and of the β parameters are given in parentheses. The resonant energy has been reported by reference [37] as 247.669 eV. In addition to the values displayed for the individual j-levels, their averaged sum per LS term is shown in bold. See text for details.

Final State $3p^4nl$		Relative Intensity : $2p_{1/2} \rightarrow 4d$	β Parameters : $2p_{1/2} \rightarrow 4d$
No	LS-term	I (θ) This work	β This work
15a	$3p^4(^1S)3d^2D_{5/2}$	12.8(2.5)	0.53(.06)
15b	$3p^4(^1S)3d^2D_{3/2}$	109.0(6.3)	-0.58(.06)
15a,b	**$3p^4(^1S)3d^2D_{5/2,3/2}$**	**121.8(7.6)**	**-0.46(.03)**
16a	$3p^4(^3P)5s^4P_{5/2}$	8.6(2.3)	-0.68(.04)
16b	$3p^4(^3P)5s^4P_{3/2}$	-	-
16c	$3p^4(^3P)5s^4P_{1/2}$	12.0(1.9)	-0.61(.04)
16a,b,c	**$3p^4(^3P)5s^4P_{5/2,3/2,1/2}$**	**20.6(0.9)**	**-0.64(.04)**
17a	$3p^4(^3P)5s^2P_{3/2}$	-	-
18a	$3p^4(^3P)4d^4D_{7/2}$	-	-
18b	$3p^4(^3P)4d^4D_{5/2}$	-	-
17b	$3p^4(^3P)5s^2P_{1/2}$	-	-
17a,b	**$3p^4(^3P)5s^2P_{3/2,1/2}$**	**-**	**-**
18c	$3p^4(^3P)4d^4D_{3/2}$	19.6(2.2)	-0.50(.03)
19	$3p^4(^1D)3d^2S_{1/2}$	113.0(6.9)	1.83(.16)
18d	$3p^4(^3P)4d^4D_{1/2}$	-	-
18a,b,c,d	**$3p^4(^3P)4d^4D_{7/2,5/2,3/2,1/2}$**	**19.6(2.2)**	**-0.50(.03)**
20a	$3p^4(^3P)4d^4F_{9/2}$	8.7(2.6)	1.36(.14)
20b	$3p^4(^3P)4d^4F_{7/2}$	12.8(2.8)	-1.00(.05)
21a	$3p^4(^3P)4d^4P_{1/2}$	20.2(1.9)	0.04(.03)
20c	$3p^4(^3P)4d^4F_{5/2}$	-	-
20a,b,c	**$3p^4(^3P)4d^4F_{9/2,7/2,5/2}$**	**21.5(2.8)**	**-0.04(.03)**
21b	$3p^4(^3P)4d^4P_{3/2}$	7.1(3.3)	*
22a	$3p^4(^3P)4d^2F_{7/2}$	19.7(1.9)	-1.00(.05)
21c	$3p^4(^3P)4d^4P_{5/2}$	3.8(0.8)	1.37(.16)
21a,b,c	**$3p^4(^3P)4d^4P_{5/2,3/2,1/2}$**	**31.1(2.5)**	**1.01(.11)**
22b	$3p^4(^3P)4d^2F_{5/2}$	7.5(2.1)	-1.00(.05)
22a,b	**$3p^4(^3P)4d^2F_{7/2,5/2}$**	**27.2(3.5)**	**-1.00(.05)**
23a	$3p^4(^3P)4d^2P_{1/2}$	42.6(2.9)	-0.27(.03)
23b	$3p^4(^3P)4d^2P_{3/2}$	57.4(3.8)	-0.62(.04)
23a,b	**$3p^4(^3P)4d^2P_{3/2,1/2}$**	**100.0**	**-0.47(.03)**
24	$3p^4(^3P)4d^2D_{5/2,3/2}$	238(13)	0.06(.03)
25	$3p^4(^3P)5s^2D_{5/2,3/2}$	37.3(2.6)	- 0.72(.04)
25a	$3p^4(^1D)4d^2G_{9/2}$	25.3(2.0)	0.30(.04)
25b	$3p^4(^1D)4d^2G_{7/2}$	12.2(2.3)	0.58(.06)
25a,b	**$3p^4(^1D)4d^2G_{9/2,7/2}$**	**37.5(3.1)**	**0.44(.06)**
26a	$3p^4(^3P)6s^4P_{5/2}$	-	-
26b	$3p^4(^3P)6s^4P_{3/2,1/2}$	8.2(2.2)	-1.00(.05)
26a,b	**$3p^4(^3P)6s^4P_{5/2,3/2,1/2}$**	**8.2(2.2)**	**-1.00(.05)**
27	$3p^4(^1D)4d^2D_{5/2,3/2}$	135.7(8.3)	-0.25(.03)
28	$3p^4(^1D)4d^2P_{3/2,1/2}$	240(14)	0.20(.04)

* Large positive β value.

Table 8. Experimental relative intensities (measured at the magic angle) and β parameters for the Ar $2p_{1/2}^{-1}4d$ resonance. The uncertainties of the intensities and of the β parameters are given in parentheses. The resonant energy has been reported by reference [37] as 249.819 eV. In addition to the values displayed for the individual j-levels, their averaged sum per LS term is shown in bold. See text for details.

V. Conclusions

One of the most powerful tools currently used to unmask nature and reveal the deep inner-shell structure of atoms and molecules is synchrotron radiation. This technology, now entering into its fourth decade, has gone through a series of improvements and has now just crossed another threshold, allowing for photon fluxes of greater than 10^{13} photons per second with an energy resolution less than 0.1%. Atomic physicists are now only beginning to understand the full advantages of this tool. Researchers are now able to perform more detailed studies of atoms engaging in a number of processes, such as photoexcitation or photoionization.

This thesis has presented a study of inner-shell electron excitations of the noble gas argon. By using time-of-flight spectroscopy to measure the distribution of resonant Auger electrons from argon atoms photoexcited with synchrotron radiation, quantitative data were collected revealing the relative probabilities of decay to various final excited states (the relative intensities) as well as the angular distributions (β parameters) of the ejected electrons. Since these data were taken using a newly available third generation synchrotron source, many of the measurements were first made with this study. Specifically, the angular distributions of the $2p^{-1}3d$ and $2p^{-1}4d$ resonances and the intensity distributions for the $2p_{1/2}^{-1}4d$ resonance were reported for the first time through this effort [32].

These results confirm previous reports that the spectator model of Hergenhahn et. al. [10] accurately describes the intensity distributions and β parameters for the $2p^{-1}4s$ resonance [10], although superior agreement was found between the experimental data and the calculations made by Chen [12], who used the MCDF method with intermediate coupling and configuration interaction. For both intensity and angular distributions, models treating the $2p^{-1}4s$ resonant Auger decays as a two step process produce the most accurate results.

For each of the resonances studied ($2p_{1/2,3/2}^{-1}4s$, 3d, and 4d) the reported β parameters for most of the final ionic states were small positive values or negative values, indicating a preferred electron ejection isotropically or perpendicular to the electric field, respectively. This result demonstrates the enhanced population of parity unfavored states that can be reached through resonant Auger processes [46]. Furthermore, this result corroborates the theoretical work of Cooper [9]. In addition, for each of the three resonances, it was found that although the relative intensity distribution for resonances from the two different spin orbit states ($2p_{1/2}$ and $2p_{3/2}$) were not necessarily very similar, the extracted β values for the final ionic states did show agreement for the two resonances in most cases.

It is hoped that this work will help theoretical atomic physicists with their current models, and that as a result of this work further experimental and theoretical work will be stimulated.

VI. References

[1] L. Lederman, *The God Particle*, Houghton Mifflin Company (1993).

[2] D. Ebbing, *General Chemistry, 3e*, Houghton Mifflin Company (1990), pp. 40-41.

[3] R. Serway, C. Moses, & C. Moyer, *Modern Physics*, Saunders College Publishing (1989), pp. 87-107.

[4] Taken from *Advanced Light Source Activities Report 1995*, prepared by the Advanced Light Source, Lawrence Berkeley National Laboratory (1996).

[5] R. Eisberg & R. Resnick, *Quantum Physics of Atoms, Molecules, Solids, Nuclei, and Particles*, John Wiley and Sons (1974), p. 49.

[6] J. Eland, *Photoelectron Spectroscopy*, Butterworths (1974), p. 2.

[7] B. Langer, A. Farhat, B. Nessar, N. Berrah, O. Hemmers, & J. D. Bozek, in proceeding of "Atomic Phyiscs with hard X-rays from high Brilliance Synchrotron Light Sources," Argonne National Laboratory, 20-21 May, 1996.

[8] J. Berkowitz, *Photoabsorption, Photoionization, and Photoelectron Spectroscopy*, Academic Press (1979).

[9] J. W. Cooper, *Phys. Rev. A* **39**, 3714 (1989).

[10] U. Hergenhahn, N. M. Kabachnik, & B. Lohmann, *J. Phys. B: At. Mol. Opt. Phys.* **24**, 4759 (1991).

[11] M. H. Chen, *Phys. Rev. A* **45**, 1684 (1992).

[12] M. H. Chen, *Phys. Rev. A* **47**, 3733 (1993).

[13] M. Meyer, E. von Raven, M. Richter, B. Sonntag, & J. E. Hansen, *J. Electron Spectrosc. Relat. Phenom.* **51**, 407 (1990).

[14] H. Derenbach & V. Schmidt, *J. Phys. B: At. Mol. Opt. Phys.* **17**, 83 (1984).

[15] B. Langer, "Analyzing Photoelectron Data," (1995, unpublished).

[16] U. Becker, D. Szostak, M. Kupsch, H. G. Kerkhoff, B. Langer, & R. Wehlitz, *J. Phys. B: At. Mol. Opt. Phys.* **22**, 749 (1989).

[17] H. Aksela, S. Aksela, G. M. Bancroft, K. H. Tan, & H. Pulkkinen, *Phys. Rev. A* **33**, 3867 (1986).

[18] U. Becker, T. Prescher, E. Schmidt, B. Sonntag, & H. E. Wetzel, *Phys. Rev. A.* **33**, 3891 (1986).

[19] P. A. Heimann, D. W. Lindle, T. A. Ferrett, S. H. Liu, L. J. Medhurst, M. N. Piancastelli, D. A. Shirley, U. Becker, H. G. Kerkhoff, B. Langer, D. Szostak, & R. Wehlitz, *J. Phys. B: At. Mol. Opt. Phys.* **20,** 5005 (1987).

[20] B. Kammerling, B. Krassig, & V. Schmidt, *J. Phys. B: At. Mol. Opt. Phys.* **23**, 4487 (1990).

[21] H. Aksela, S. Aksela, H. Pulkkinen, G. M. Bancroft, & K. H. Tan, *Phys. Rev. A* **37**, 1798 (1988).

[22] T. A. Carlson, D. R. Mullins, C. E. Beall, B. W. Yates, J. W. Taylor, D. W. Lindle, & F. Grimm, *Phys. Rev. A* **39**, 1170 (1989).

[23] M. Meyer, E. von Raven, B. Sonntag, & J. E. Hansen, *Phys. Rev. A* **43**, 177 (1991).

[24] J. Mursu, H. Aksela, O-P Sairanen, A. Kivimaki, E. Nommiste, A. Ausmees, S. Svenson, & S. Aksela, *J. Phys. B: At. Mol. Opt. Phys.* **29**, 4387 (1996).

[25] M. Meyer, E. von Raven, B. Sonntag, & J. E. Hansen, *Phys. Rev. A* **49**, 3685 (1994).

[26] H. Aksela & J. Mursu, *Phys. Rev. A* **54**, 2282 (1996).

[27] R. Camilloni, M. Zitnik, C. Comicioli, M. Zacchigna, C. Crotti, C. Ottaviani, C. Quaresima, P. Perfetti, & G. Stefani, *Phys. Rev. Lett.* **77**, 2646 (1996).

[28] J. A. de Gouw, J. van Eck, A. C. Peters, J. van der Weg, & H. G. M. Heideman, *J. Phys. B: At. Mol. Opt. Phys.* **28**, 2127 (1995).

[29] C. D. Caldwell, in *proceedings from* "15th international conference on X-Ray and Inner-shell Processes," edited by T. A. Carlson, M. O. Krause, & S. T. Manson (AIP, Knoxville, 1990), p. 685.

[30] B. Langer, N. Berrah, A. Farhat, O. Hemmers, & J. D. Bozek, *Phys. Rev. A* **53**, R1946 (1996).

[31] C. D. Caldwell & S. Hallman, *Phys. Rev. A* **53**, 3344 (1996).

[32] A. Farhat, M. Humphrey, B. Langer, N. Berrah, & J. Bozek, submitted to *Phys. Rev. A* (1997).

[33] Taken from *An ALS Handbook*, prepared by the Advanced Light Source, Lawrence Berkeley National Laboratory (1989).

[34] B. Craseman, in proceedings of from "XVII International Conference on the Physics of Atomic Collisions," 10-16 July, 1991.

[35] F. Wuilleumier, from *Review of Fundamental Processes and Applications of Atoms and Ions,* C. D. Lin, ed., World Scientific (1993).

[36] M. G. White, R. A. Rosenberg, G. Gabor, E. D. Poliakoff, G. Thornton, S. H. Southworth, & D. A. Shirley, *Rev. Sci. Instr.* **50**, 1268 (1979).

[37] G. C. King, M. Tronc, F. H. Read, & R. C. Bradford, *J. Phys. B* **10**, 2479 (1977).

[38] L. Minnhagen, *Arkiv Fur Fys.* **25**, 203 (1963).

[39] P. B. Bevington & D. K. Robinson, *Data Reduction and Error Analysis for the Physical Sciences, 2ed*, McGraw Hill (1992), Chapter 3.

[40] B. Langer, J. Viefhaus, O. Hemmers, A. Menzel, R. Wehlitz, & U. Becker, *Phys. Rev. A* **51**, R882 (1995).

[41] A. Menzel, PhD Thesis, Technische Universitat Berlin (1990, unpublished).

[42] N. Berrah, private communication.

[43] M. Meyer, PhD Thesis, Universitat Hamburg (1990, unpublished).